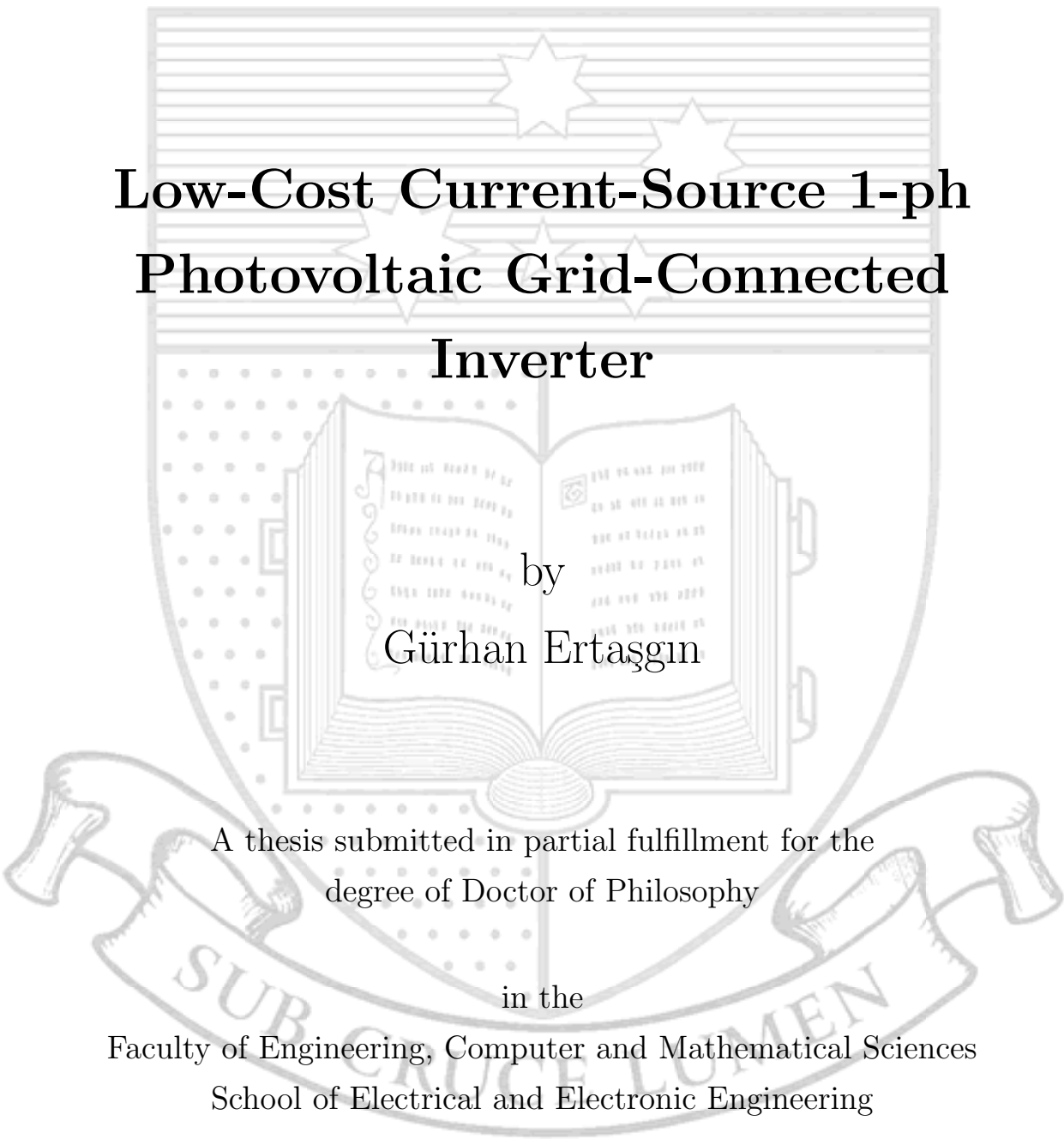


THE UNIVERSITY OF ADELAIDE

The background of the cover features a large, faint watermark of the University of Adelaide crest. The crest is a shield-shaped emblem. At the top, it has a banner with the motto 'SUB CRUCE LUMEN'. Below the banner is a shield divided into four quadrants. The top-left quadrant contains a star, the top-right a smaller star, the bottom-left a grid of dots, and the bottom-right an open book. The book's pages are filled with text, and a quill pen is positioned at the bottom center of the book. The entire crest is rendered in a light gray color.

**Low-Cost Current-Source 1-ph
Photovoltaic Grid-Connected
Inverter**

by
Gürhan Ertasgin

A thesis submitted in partial fulfillment for the
degree of Doctor of Philosophy

in the

Faculty of Engineering, Computer and Mathematical Sciences
School of Electrical and Electronic Engineering

August 2010

CHAPTER 1

INTRODUCTION

This chapter introduces photovoltaic (PV) electrical energy generation systems. The principles of PV energy conversion with common grid-connected power converters are discussed, and a low-cost grid-connected PV inverter topology is introduced. The chapter concludes with the aims of the research project, discusses its original contributions and describes the structure of the thesis.

1.1 Renewable Energy Sources

The world's energy consumption has been increasing significantly. Fossil fuels are presently the primary source of energy however the fossil fuel reserves are finite and their use produces carbon dioxide (linked to global warming) and causes pollution. There has thus been considerable interest in renewable energy sources primarily in wind and solar. These sources however, require converter systems to obtain a useful energy, which have many similarities.

Wind Energy

Fig. 1.1 shows a conventional wind turbine power conditioning system. Wind turbines

capture energy from the wind by means of aerodynamically designed blades which convert it to rotating mechanical power. The generator converts the mechanical power into electrical energy. The rectifier converts the variable-frequency, variable-voltage AC from the generator into DC. An inverter is then used to convert this to constant-frequency AC power which is fed into the power grid usually via filter.

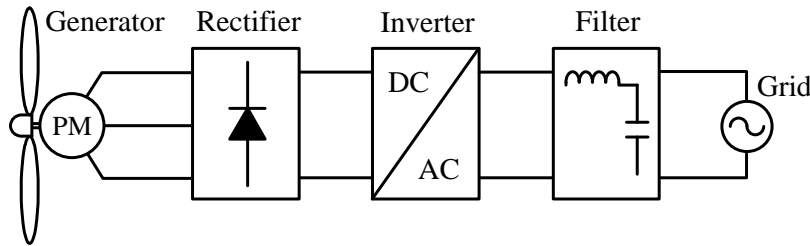


FIGURE 1.1: *Block diagram of a typical wind turbine power conditioning system.*

Photovoltaic Energy

The typical efficiency of conversion from solar power to electrical power is in the range 13 to 16% [1]. Photovoltaic cells use semiconductor technology to transform the energy in sunlight into electricity. Silicon is the most widely used semiconductor material in PV cell, which consists of a junction consisting of n and p-doped silicon (see Fig. 1.2(a)). When light (photons) strikes the junction, the energy in the photons is converted to electric power.

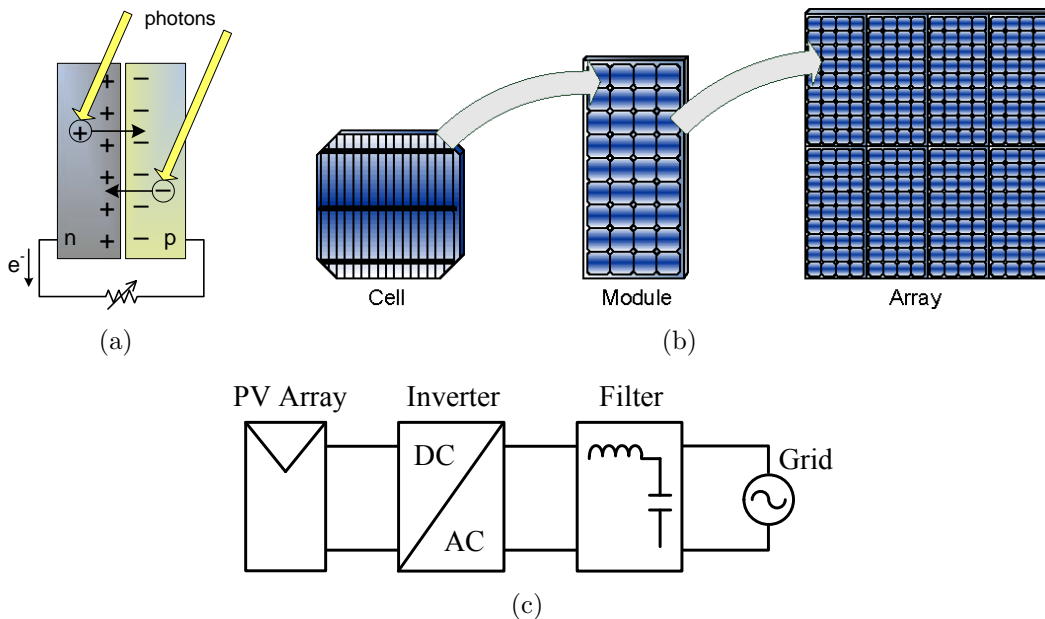


FIGURE 1.2: (a) *Principle of producing electricity from sunlight* (b) *PV cell, module and array structures* (c) *block diagram of a typical PV power conditioning system.*

Unlike the wind turbines, PV cells do not have moving parts which gives them a longer life time with little maintenance, and they became very competitive as their costs have also declined substantially over time [2].

As shown in Fig. 1.2(b) a group of PV cells can be connected in series or parallel to generate more power which are usually mounted in a protective frame to form what is called a PV module or panel.

Fig. 1.2(c) shows a common PV power conditioning system. The obtained DC power from the PV array is converted to AC power which is fed into the grid via filter similar to wind power system in Fig. 1.1.

1.2 Power Electronics Control

Due to the high initial cost of PV arrays, it is important to utilize them effectively and extract the maximum possible power. As PV arrays produce a DC output, PV systems use an inverter for the DC/AC conversion (see Fig. 1.2(c)). The inverter converts the DC input power into AC output power and controls the PV module in order to maximise the output power.

1.2.1 Stand-Alone and Grid-Connected Inverters

Inverters can be classified as stand-alone or grid-connected. Stand-alone inverters directly drive AC powered loads, e.g. a refrigerator. Battery energy storage is often used with stand-alone systems so that power is available during the night. Grid-connected inverters however, feed power back into the power grid and does not need to include battery storage (see Fig. 1.3(b)) In effect, the grid acts as an energy storage system. Due to grid connection, such inverters must meet tight technical standards (discussed in Section 1.4) for correct operation with the grid. Therefore they are more complex and expensive than stand-alone inverters. This thesis will consider a grid-connected inverter topology to offer a low-cost solution.

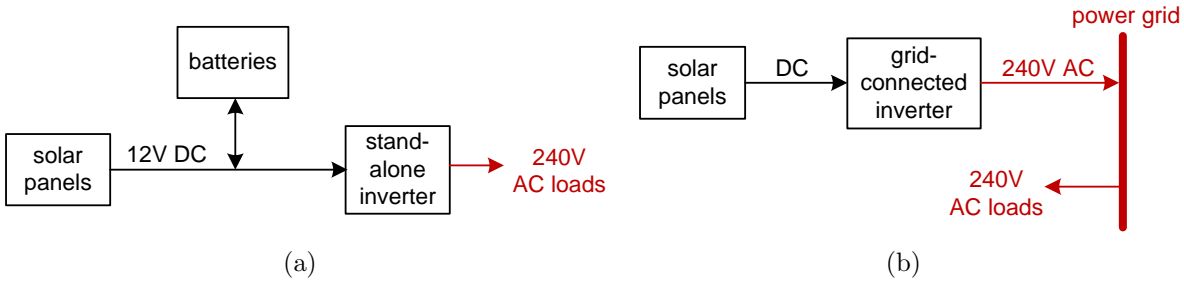


FIGURE 1.3: (a) *Stand-alone system block diagram* (b) *Grid-connected system block diagram*.

1.3 Grid-Connected Inverter Topologies

Grid-connected inverters can also be classified according to their commutation type as either line-commutated and self-commutated [3, 4]. The line-commutated inverters' key point is that their switching frequency is controlled from the line current, which is usually controlled by a thyristor. However the thyristor requires auxiliary commutation circuit to reduce the current to zero. Although the thyristor based line-commutated inverters were popular in the past they are not preferred due to the requirement of additional filtering elements. The self-commutated inverters however control their turn-on and turn-off timing by using high-frequency easy to control switching devices such as MOSFETs and IGBTs. The self-commutated inverters are classified as voltage-source (VSI) and current-source (CSI) as illustrated in Fig. 1.4 [3].

1.3.1 Voltage Source Inverters

Most research in single-phase GC PV inverters have been based on a current-controlled voltage-source inverter. In such inverters, the instantaneous waveform of the current to be output is applied as the reference value and a high power factor can be obtained by a simple PWM control [3].

Inverters are desired to have high output power quality, high efficiency, high reliability, low cost, and simple circuitry. Single-phase photovoltaic VSIs employ a large DC link capacitor (see Fig. 1.4(a)) due to resulting pulsating output power. It can be noted that the VSI topology tends to be slightly cheaper and more efficient than the CSI topology as the DC link capacitor has lower losses and has lower cost than the DC link inductor

used in a CSI [2]. However the large DC link capacitor has a reliability issue for VSIs being the main lifetime-limiting component [5]. Compared to single-phase inverters, three-phase VSIs have constant power flow, which results in a reduced DC link capacitor requirement.

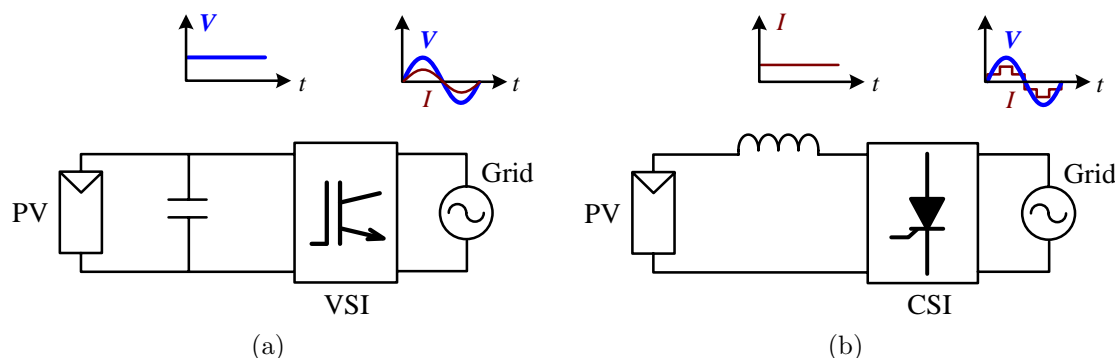


FIGURE 1.4: (a) *Common single-phase voltage-source inverter*, (b) *early single-phase current-source inverter*.

1.3.2 Current Source Inverters

The CSI is well known from high-power drives and rectifiers, but it is rarely considered in low and medium-power ranges [6–8]. CSIs have a large series inductor which maintains constant current across the DC link. Early GCIs were of the current-source type which used a DC link inductor to produce a constant-current source and line-frequency commutated switches to produce a square-wave output current, as seen in Fig. 1.4(b). Although, this concept is simple, the output current required substantial filtering to meet the grid harmonic standards [9].

The present CSI inverters can offer simpler control requirements and also avoid the need for a DC link capacitor. A grid-connected PV CSI has advantages as follows :

- It is easier for a PWM CSI to supply sinusoidal current output which has unity power factor,
- there is no need for an output sensor or any feedback control to connect the inverter with the grid line in the CSI and

- a short-circuit failure causes no excessive current in the CSI as the DC current never exceeds the PV panel short-circuit current [10].

On the other hand the DC link inductor losses, size, weight and cost are important concerns.

This thesis will consider a current-source inverter and will address the limitations of such system during grid-connected operation.

1.4 Technical Requirements

Various technical requirements are compulsory due to standardisation [9, 11] for small grid-connected renewable generation systems connected via inverters. Two of these requirements are, the total harmonic distortion (THD) and power factor (PF), which need to be between certain limits. In addition such inverters require fault protection against islanding. That is, if the grid is disconnected for some reason, the inverter should not maintain supply outside the consumer's installation as the safety of both the public and utility staff may be compromised. Furthermore grounding, DC injection protection and electromagnetic interference limitation should also be taken into account for the grid connection.

1.4.1 Total Harmonic Distortion

The total harmonic distortion is defined as the ratio of the root mean square (rms) value of the signal composed of all harmonics and the rms value of the first harmonic, and it is usually given by percentage.

$$\text{THD}(\%) = \frac{\sqrt{\sum_{n=2}^{\infty} H_n^2}}{H_1} \times 100 \quad (1.1)$$

where H_n is the rms value of the n^{th} harmonic and H_1 is the rms value of the first harmonic [11].

Australia has adopted the same harmonic limits as adopted in the US IEEE P929 [12]. Thus the total harmonic distortion should be less than 5% at the rated inverter output power. Table 1.1 shows the detailed THD limits of the Australian Standard [9].

TABLE 1.1: *Current Harmonic Limits*

Harmonic Order	Limit for each harmonic based on % of fundamental
2 - 9	4%
10 - 15	2%
16 - 21	1.5%
22 - 33	0.6%
Even harmonics	25% of equivalent odd harmonics
Total harmonic distortion (THD) to the 50th harmonic	5%

1.4.2 Power Factor

Power factor is a figure of merit that measures how efficiently energy is transmitted and is defined as the ratio of the active power P to the apparent power S . A value of unity is desired for the power factor, both at the grid connection as well as at the inverter output. From the definition of the THD in (1.1), the rms value of distorted current equals

$$I_{rms} = \sqrt{\sum_{n=1}^{\infty} I_n^2} \quad (1.2)$$

where I_n is the amplitude of the harmonic current of n^{th} order. In addition the following relationship can be derived between the current THD and rms current :

$$I_{rms} = I_1 \sqrt{1 + \text{THD}^2} \quad (1.3)$$

Using the above definition the sinusoidal waveform power factor definition can be generalised to take harmonic currents into account as well, utilising the THD of the current only [13] :

$$PF = \frac{P}{S} = \frac{I_1 \cos \varphi}{I_{rms}} = \frac{\cos \varphi}{\sqrt{1 + \text{THD}^2}} \quad (1.4)$$

where φ is the phase difference between the fundamental current and voltage. The power factor of the inverter, considered as a load from the perspective of the grid, should be in the range from 0.8 leading to 0.95 lagging for all output from 20% to 100% of rated output power [9].

1.5 Literature Review of CSIs

1.5.1 Line-Commutated CSI

One of the first line-commutated CSI topologies was reported in [14] which has a voltage source load with series inductance. The CSI circuit given in Fig. 1.5 is based on the well-known parallel inverter with the addition of series diodes to trap the charge on the commutating capacitor, enabling operation with an AC load of any power factor. In this circuit the thyristors T_1 and T_2 conduct alternately for a period of 180° electrical and they are gated at the same frequency as the back emf of the load but are fired at a delay angle with respect to the zero crossing of the back emf. The advantage of this circuit is the zero-current switching scheme that effectively eliminates switching losses. Therefore only conduction losses should be considered. However if it is the grid, the inverter output current i_a resembles a squarewave and requires considerable filtering that increases the cost and reduces efficiency.

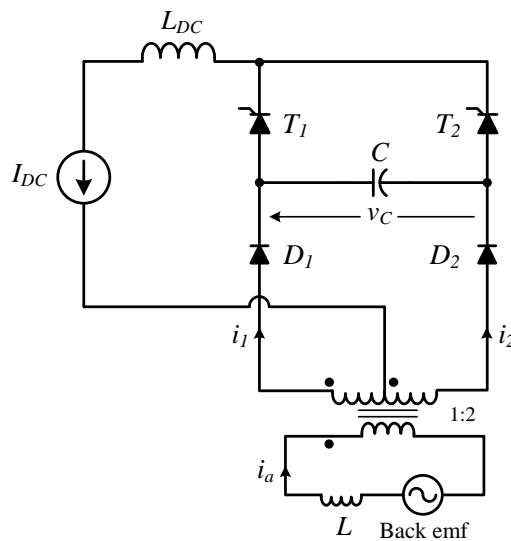


FIGURE 1.5: *Early CSI which uses parallel inverter topology with the addition of series diodes.*

1.5.2 Self-Commutated CSI

A widely known single-phase H-bridge circuit configuration is shown in Fig. 1.6 which uses IGBTs as the high-frequency switching components [15]. As the DC link inductor has significant losses (copper and iron), pulse area modulation is introduced to reduce the size of the inductor. This modulation approach is similar to feedforward compensation control. Despite the less distorted inverter output current i_u the efficiency of the inverter is reduced significantly due to the small DC link inductor. In addition to this the number of components are increased in the main current path reducing the efficiency due to additional series diodes with IGBTs. Series diodes are needed with asymmetric voltage blocking devices such as IGBTs and MOSFETs to allow current conduction in one direction only for current-source inverters.

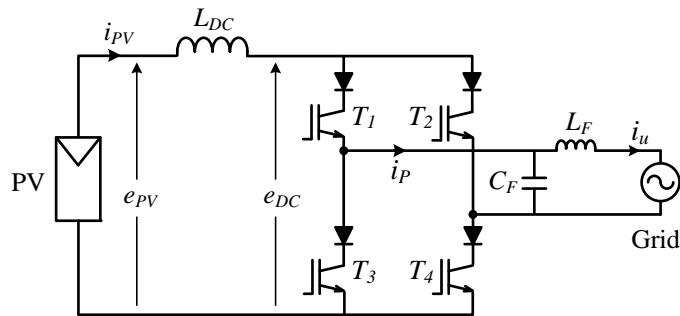


FIGURE 1.6: A single-phase H-bridge CSI using series diode-transistor arrangement.

Some recent interest has been reported in the use of PWM controlled CSIs. Fig. 1.7 shows a GTO based H-bridge grid-connected CSI [16, 17]. Although the switching loss of the GTOs are relatively high [18] they can block reverse voltage and hence eliminate the need for a series diode used in Fig. 1.6. However due to the limited switching speeds of GTOs this approach has used mainly at higher output powers. More commonly, GTO devices have been adopted in multilevel VSI systems. As expected the input DC link inductor losses in this topology were found to cause a significant reduction in the inverter efficiency.

Another self-commutated photovoltaic CSI, which uses IGBTs, is illustrated in Fig. 1.8 [19]. This topology uses two auxiliary switches which are added to the single-phase H-bridge inverter. Control of the switches was implemented by using two PWM patterns for auxiliary (S_5 and S_6) and main switches (S_1, S_2, S_3 and S_4). The auxiliary switch S_5

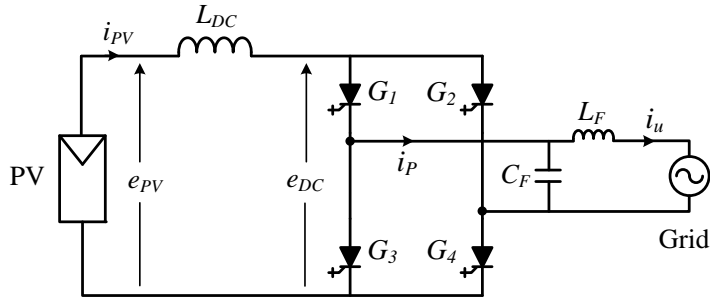


FIGURE 1.7: *GTO based H-bridge current-source inverter.*

is turned on when both positive side main switches S_1 and S_2 are off and likewise, the auxiliary switch S_6 is turned on when both negative side main switches S_3 and S_4 are off. Therefore DC current is converted into sinusoidally pulse-width modulated pulse trains. The carrier frequency harmonic contained in the pulse trains is mostly blocked by the filter reactor L_F from flowing into the grid, and most of the harmonic flows into the filter capacitors C_F . In this manner, output current is shaped into sinusoidal waveform. The output current from the PV array is smoothed by a large DC link inductor (400mH) which has significant losses (copper and iron).

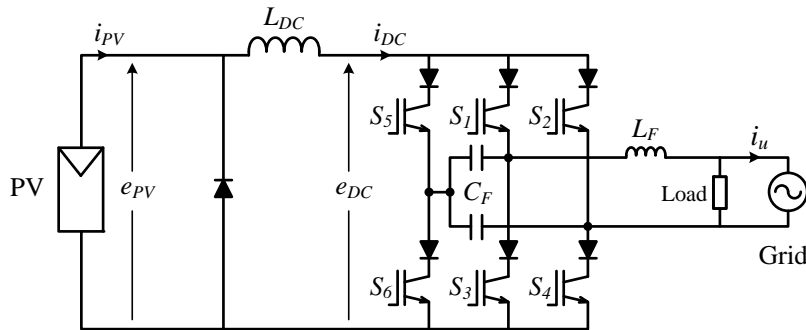


FIGURE 1.8: *Early grid-connected CSI topology.*

1.5.3 Soft-Switched CSI

An interesting single-phase current-source PV inverter topology has been proposed by Itoh and Ishizaka [20], as seen in Fig. 1.9. This is a line-commutated soft-switched CSI which uses IGBTs and diodes as a resonant switch with a thyristor H-bridge inverter. A similar topology has been introduced later with some differences in [21]. This topology uses IGBTs with series diodes instead of thyristors in the H-bridge. The first topology, with the thyristors, has a fixed voltage drop and hence less losses at higher voltages.

However the thyristor commutation (turn-off) can be a problem. Even though this concept produces a soft-switched CSI and hence improved efficiency, the inverter control is more complicated and the number of components is increased. This increases the cost of the inverter while reducing reliability.

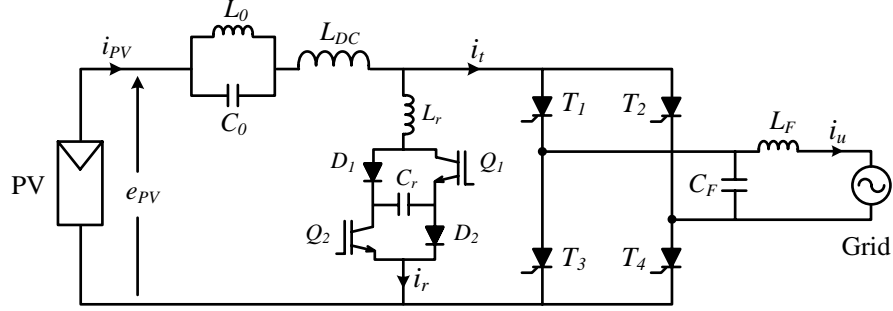


FIGURE 1.9: *Thyristor H-bridge soft-switched current-source inverter topology.*

A CSI topology was implemented based on using a high-inductance PM generator which acts as a current source, with a switched-mode rectifier (SMR) and inverter (see Fig. 1.10) [22]. In the high-inductance PM generator, the output voltage is small compared to the open-circuit voltage and hence the output current is close to the short-circuit current [10]. The machine acts as a constant-current source providing the open-circuit voltage is significantly greater than the output voltage. The combination of the uncontrolled rectifier and high inductance generator acts as a DC constant current source. The sinusoidal PWM controlled boost switch acts as a current waveshaper (CWS) [23]. Then a line-commutated inverter, including a low-pass filter, generates a sinusoidal output current which is synchronised with the grid. The main advantages of this topology are : simplified circuit topology and control requirements; the elimination of the large DC link inductor and unreliable DC link capacitor; the potential to operate over a wide wind speed range and the zero-crossing switched H-bridge unfolding circuit.

1.5.4 Three-Phase CSI

A three-phase grid-connected CSI design has been analysed by Sahan et. al [24]. As shown in Fig. 1.11 the three-phase PWM CSI is composed of a bridge which consists of MOSFETs with series diodes. A transient voltage suppressor diode D_Z in this circuit provides a “freewheeling” path in the event of an unintended open-circuit of the inverter.

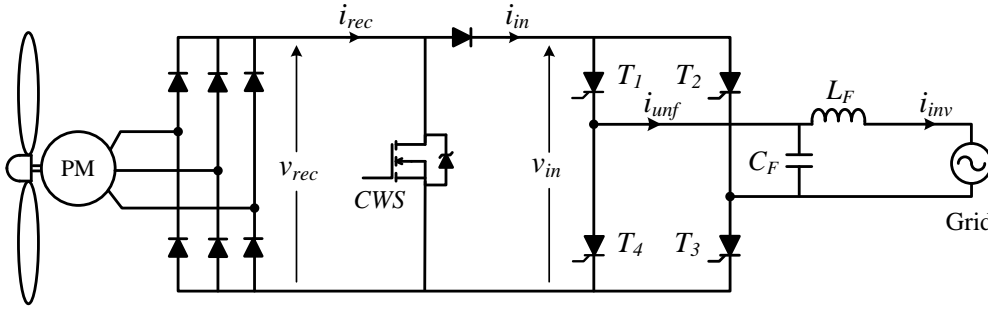


FIGURE 1.10: *Current-source grid-connected wind inverter topology using a high inductance PM machine.*

Due to its three-phase nature, the large DC link inductor was reduced in size owing to the more constant instantaneous output power.

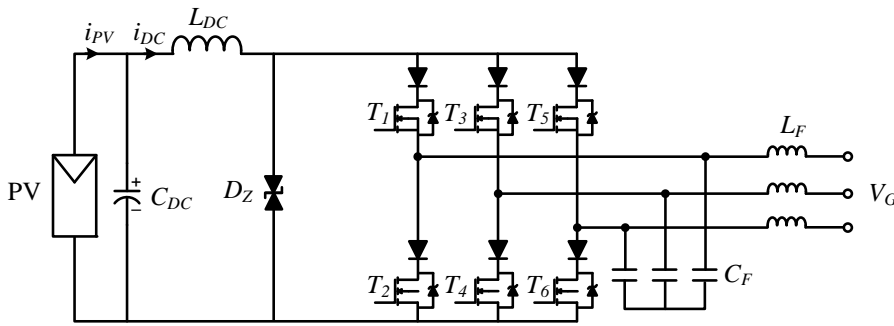
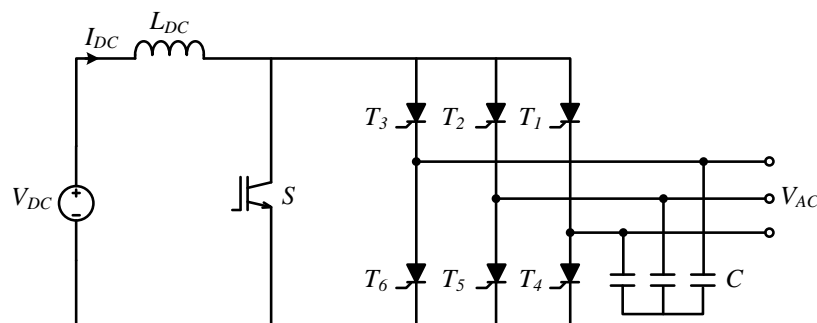


FIGURE 1.11: *Current-source three-phase inverter topology.*

A three-phase current-source boost inverter topology is reported in [23] (see Fig. 1.12). A DC voltage source and DC link inductor provide the current-source input current. The inverter itself is fundamentally line-commutated as in [14]. The key difference is that an additional parallel-connected IGBT is used and is controlled with a high-frequency PWM signal similar to [22]. This allows the thyristors to commute naturally. However, the IGBT in this topology is not soft-switched, which might cause significant switching loss.

The advantage of the above circuit is that rugged, high-power, low-cost thyristors are used for the H-bridge components. The high-frequency PWM switching implies the size of the DC link inductor and output filter capacitors can be reduced in size, and that the output current harmonic contents can be well controlled [23]. In addition, the use of thyristors avoids the need for series-connected reverse-blocking diodes.

FIGURE 1.12: *Current-source boost inverter topology.*

1.6 Research Gap

The existing literature in terms of single-phase grid-connected PV current-source inverters shows that the efficiency is the biggest concern due to the high losses in the DC link inductor. A different modulation approach was introduced to reduce the size of the inductor. However the PV array output power was reduced due to single-phase power fluctuations.

To increase efficiency, soft-switching schemes were introduced [20, 21] with resonance switches. However it increased the number of components on the main current path whilst reducing reliability and increasing cost. In addition there are still DC link inductor losses.

Other approaches try to reduce the components in the current path. However as a result the control complexity is generally increased [16, 17]. The control scheme can be simplified by using two-stage or multi-stage inverters where a DC/DC converter is responsible for maximum power point tracking (MPPT).

Consequently to overcome the stated shortcomings of the single-phase current-source inverters a different topology approach with minimum components is proposed in this research along with the optimised DC link inductor. Similar to [22], this circuit topology is an extension of the SMR circuit that was proposed for automotive applications [25], where it acted as a DC/DC converter.

In this research, instead of an uncontrolled rectifier which is fed by a high inductance PM generator as in Fig. 1.10, the constant current source is realised by a DC link inductor

connected in series with the PV panels. The topology of the proposed inverter with feedforward control is given in Fig. 1.13.

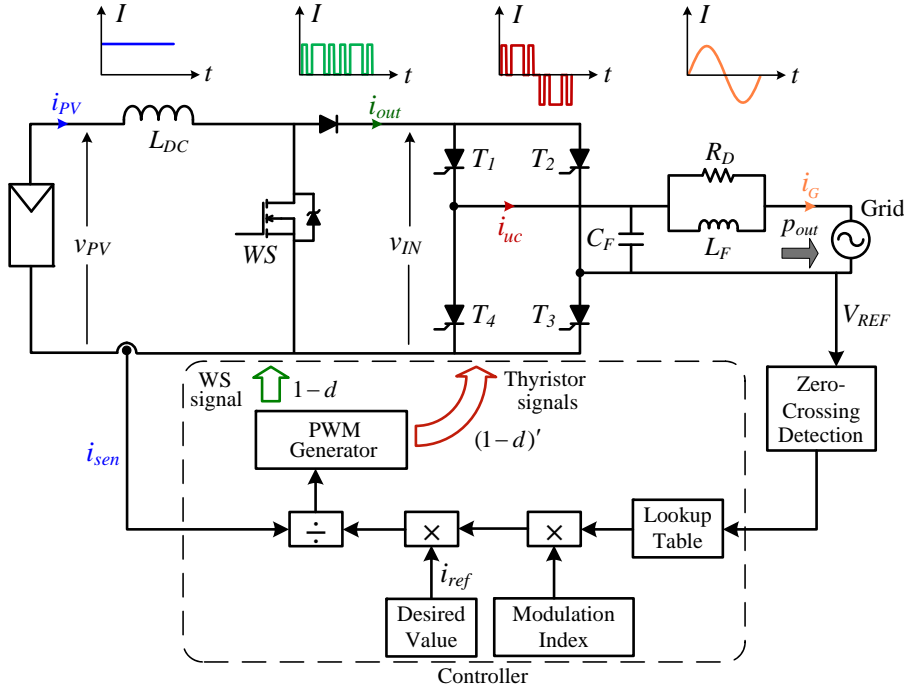


FIGURE 1.13: *Grid-connected current source inverter with feedforward control and ideal current waveforms.*

The PV array output is simulated with an alternative experimental technique called the “dark I-V test” was used to simulate sunlight operation of the PV cells [26]. The advantage of this arrangement is the ability to conveniently simulate the PV module output over a wide range of irradiances. The DC link inductor is used to provide energy storage, i.e. a constant current i_L from the PV array with little ripple at twice the line frequency fluctuations. A high frequency waveshaper switch (WS) pulse-width modulates the output current to create a rectified (unipolar) sinewave waveform, which is unfolded (polarity reversed) into a bipolar waveform by the thyristor H-bridge inverter. A low-pass line filter (CL) is utilised to remove the PWM components to produce a sinusoidal output current.

1.6.1 Original Contributions

The original contribution for this research is the detailed investigation of a grid-connected current source inverter topology for PV applications which is based on the switched-mode rectifier (SMR). As illustrated above, the topology utilises a DC link inductor that is

optimised for the application to achieve a constant-current source. In this research, the 160 W inverter operation for open-loop and feedforward compensation control was developed, simulated and experimentally investigated. The detailed system analysis was done including :

1. The modelling of the PV array investigated including irradiance and temperature effects, the results of the non-linear (ideal diode) and four-diode approximation are compared with the manufacturers data on dark I-V test results.
2. The PV array output power reduction due to the single-phase output power fluctuations as a function of DC link energy storage is investigated for VSI and CSI inverters.
3. The simplified model of the inverter (ignoring the PWM switching and output filter) is used for a fundamental analysis of the proposed topology, this investigates parameters such as : ratio of rated PV array output voltage to peak grid voltage, DC link energy storage requirement, effect of output power variation using modulation index and irradiance changes, and feedforward control.
4. The selection and optimisation of the output filter is examined to meet the grid THD and PF requirements.
5. The above modelling approach is validated by a series of tests using a 160 W prototype.
6. A higher power (1.2 kW) grid-connected inverter is designed and simulated to show that it meets the grid requirements and it has higher efficiency than the 160 W prototype inverter.

1.7 Thesis Layout

Fig 1.14 illustrates the structure of the thesis as chapters. Brief summary of the chapters are provided.

Chapter 2 describes the PV cell models which are employed for the simulation and measurements of the proposed grid-connected current-source inverter.

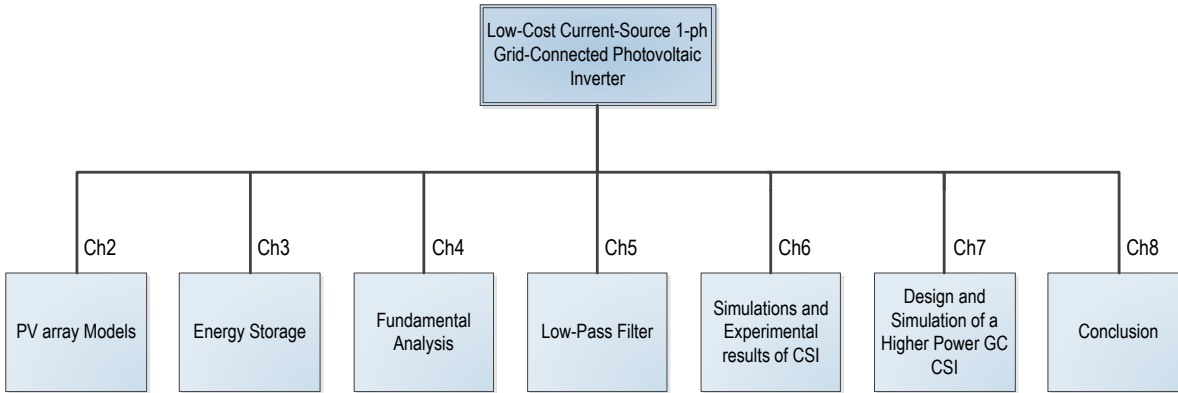


FIGURE 1.14: Thesis layout consists of chapters.

Chapter 3 analyses the relationship between the average output power reduction of PV array and the array voltage and current ripple. The relationship between the PV array output ripple and the DC link energy storage for single-phase grid-connected inverters is also described.

Chapter 4 provides the fundamental analysis, operating principles and features of a single-phase current-source grid-connected inverter. The proposed concept and its components are discussed.

Chapter 5 investigates the inverter output low-pass filter requirement. Then a specific low-pass filter topology for the proposed inverter is analysed. The analysis include THD, PF and loss studies.

Chapter 6 examines the design and testing of a 160 W single-phase current-source grid-connected PV inverter. The open-loop and feedforward controlled CSI simulation results are compared with the measurements. The evaluation of the system performance is also analysed in respect to performance indicators of THD and PF.

Chapter 7 utilises the results, from Chapters 2 to 6 to design a 1.2 kW single-phase grid-connected PV inverter to meet the THD and PF requirements and to obtain higher efficiency.

Chapter 8 summarises the results from the thesis. This chapter also includes original contributions within the work and suggestions for future work.

CHAPTER 2

PV ARRAY MODELS

This chapter describes photovoltaic (PV) cell models which are employed for simulations and measurements. These models are used for the proposed grid-connected (GC) current-source inverter (CSI). Non-linear, 4-diode and rectangular PV cell models are explained. Normalisations of these models are also introduced. The accuracy of the non-linear model is checked with experimental measurements. The dark I-V PV array test arrangement is shown to model the PV array characteristics accurately and will be used later to test the current-source inverter.

2.1 Background and PV Module Modelling

From an electrical standpoint, a solar (or PV) cell, is a diode which is optimised to absorb photons from the sun and convert them into electrical energy. The amount of solar power available per unit area is called the “irradiance” and is expressed in watts per square metre. The efficiency of a PV cell is a measure of how effectively it converts the available solar power into electrical power. The efficiency of typical practical PV cells varies between 5 and 20% and depends on the quality of the semiconductor material used, and the irradiance and temperature.

A PV module consists of a group of PV cells connected in series to increase their output voltage and power. In turn PV modules are also connected in series or parallel according to the required power output to form a PV array (see Fig. 1.2(b)).

The electrical behaviour of PV modules is normally represented by a current versus voltage curve (I-V) as seen in Fig. 2.1. As illustrated in the figure it defines three important quantities: V_{OC} , the open-circuit voltage, I_{SC} , the short-circuit current, and the maximum power point P_0 at which the product of V and I is at a maximum. This is the optimal operating point of the solar cell. The voltage and current at P_0 are V_0 and I_0 .

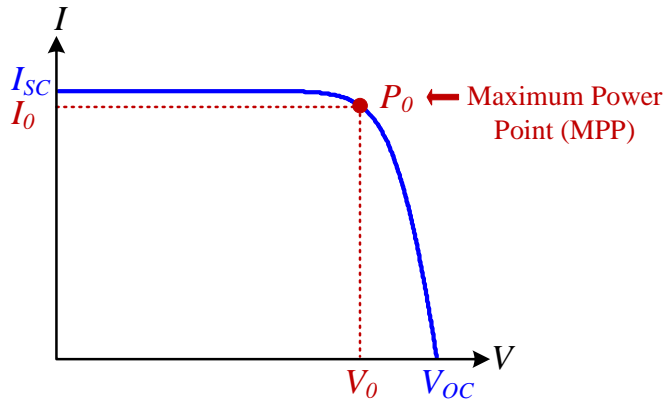


FIGURE 2.1: Typical I-V curve of a PV module which shows the open-circuit voltage (V_{OC}), short-circuit current (I_{SC}), maximum power point (P_0), voltage at MPP (V_0) and current at MPP (I_0).

The PV array used later for the CSI experiments, consists of two series-connected 80 W PV modules (BP380U) [27] which produce a total of about 160 W of output power. Table 2.1 shows the specifications of the BP380U PV module from the manufacturer under standard test conditions (STC) or nominal conditions. These conditions are : irradiance level of 1000 W/m^2 , cell or module temperature of 25°C (298 K) and the reference air mass 1.5 solar spectral irradiance distribution.

Three PV cell models are described in this section which will be used later for the grid-connected inverter simulations. The models are based on the BP380U PV module and have different complexity levels.

TABLE 2.1: Specifications of the 80 W BP Solar BP380U module at nominal conditions.

Parameter	Value
Rated Maximum Power (P_0)	80 W
Voltage at P_0 (V_0)	17.6 V
Current at P_0 (I_0)	4.55 A
Short Circuit Current (I_{SC})	4.8 A
Open Circuit Voltage (V_{OC})	22.1 V
Temperature Coefficient of I_{SC} (α)	$(0.065 \pm 0.015)\%/^{\circ}\text{C}$
Temperature Coefficient of V_{OC} (β)	$-(80 \pm 10)\text{mV}/^{\circ}\text{C}$

2.1.1 Non-linear Model

The non-linear model (see Table 2.2) is based on a diode with parallel light-induced current which is assumed equal to I_{SC} . The series (R_S) and parallel (or shunt, R_P) resistances increase the model accuracy. However R_P has a negligible effect compared to R_S and hence it is not used in this simplified model.

The non-linear model is based on the ideal diode equation, which links the diode current for a given diode voltage. Taking into account that the diode is connected in parallel to the light-induced current-source, the relationship between the PV cell output current (I) and the PV cell output voltage (V) is given by

$$I = I_{SC} - I_S \left(e^{\frac{q(V+IR_S)}{nkT}} - 1 \right) \quad (2.1)$$

where; I_S is the diode saturation current that depends on the type, doping density and junction; q is the charge on an electron; n is the diode ideality factor; k is Boltzman's constant; and T is the temperature of the PV cell. (2.1) is for a single cell and can be scaled appropriately for a module. For the module calculations R_S needs to be multiplied with the number of series resistances (N_S) in the module. Then voltage and current in (2.1) represents the module's values.

The following three equations can be used to determine the parameters in (2.1). The parameters in the first column of the Table 2.3 show the non-linear model specifications under nominal conditions.

$$I_{SC(T,G)} = I_{SC(nom)} \frac{G}{G_{nom}} (1 + \alpha (T - T_{nom})) \quad (2.2)$$

(2.2) shows that the short-circuit current (and hence power) is directly proportional to irradiance G , which is shown in the graphs of Table 2.2. The short-circuit current increases with temperature, and for the BP380U module I_{SC} changes from 25 to 75°C as seen in Table 2.4.

$$I_{S(T,G)} = \frac{I_{SC(T,G)}}{e^{\frac{qV_{OC}(T_{nom})}{n k T(T_{nom})} - 1}} \left(\frac{T}{T_{nom}} \right)^{\frac{3}{n}} e^{\frac{qV_g}{n k} \left(\frac{1}{T_{nom}} - \frac{1}{T} \right)} \quad (2.3)$$

(2.3) shows how the saturation current I_S can be calculated using (2.2) and the nominal open-circuit voltage.

$$R_S = - \left. \frac{dV}{dI} \right|_{V_{OC}} - \frac{1}{X_V} \quad \text{where,} \quad X_V = \frac{q I_S(T_{nom})}{n k T} e^{\frac{qV_{OC}(T_{nom})}{n k T_{nom}}} \quad (2.4)$$

The series resistance of the PV module has a noticeable effect upon the slope of the

TABLE 2.2: PV simulation models for the BP380U PV module and their current and power-voltage characteristics for various irradiance values. The dots in the graphs represent the MPP (P_0).

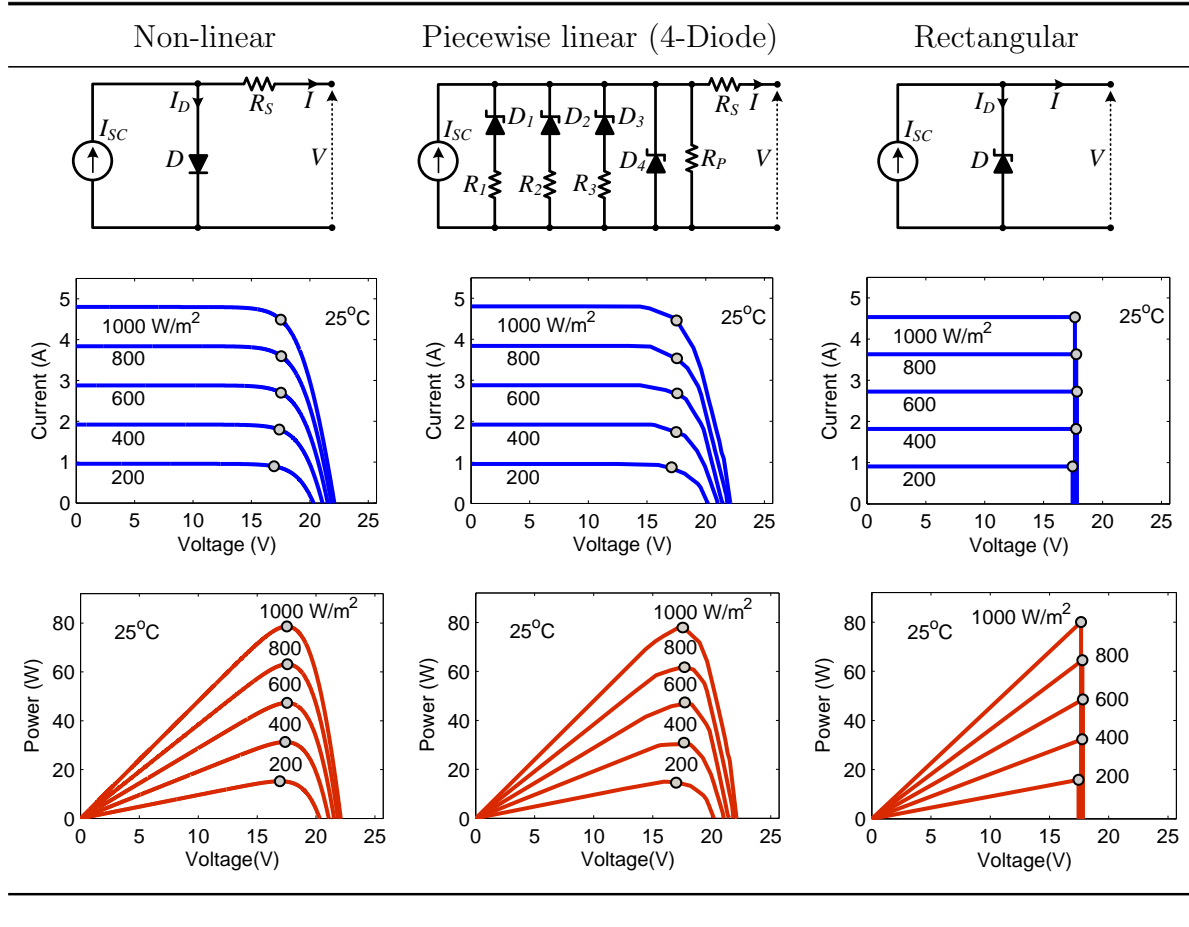


TABLE 2.3: Parameter values of the PV module models under nominal conditions.

Non-linear	Piecewise linear	Rectangular
$n = 1.02$	$I_{SC} = 4.8 \text{ A}$	$I_{SC} = 4.533 \text{ A}$
V_g (band gap V.) = 1.21 V	$D_1 = 18.5 \text{ V}$	$D = 17.66 \text{ V}$
N_S (module cell number) = 36	$D_2 = 21.5 \text{ V}$	
k (Boltzman constant) = $1.38 \times 10^{-23} \text{ J/K}$	$D_3 = 22.75 \text{ V}$	
q (charge on an electron) = $1.60 \times 10^{-19} \text{ C}$	$D_4 = 23.5 \text{ V}$	
$R_S = 10.5 \text{ m}\Omega$	$R_1 = 8 \text{ }\Omega$	
	$R_2 = 2 \text{ }\Omega$	
	$R_3 = 0.5 \text{ }\Omega$	
	$R_P = 100\text{k } \Omega$	
	$R_S = 0.5 \text{ }\Omega$	

I-V curve at $V = V_{OC}$ and can change the MPP significantly. In order to obtain R_S , (2.1) is differentiated and evaluated at the term $(dV/dI)|_{V_{OC}, I=0}$ and rearranged in terms of R_S [28, 29] to yield (2.4). The slope of the voltage-current curve which can be obtained from the PV module manufacturer data sheet. The natural slope of the ideal diode equation corresponds to the second part of the (2.4). Consequently the difference between the natural slope of the ideal diode equation and the slope from the module data sheet gives the module resistance R_S .

In addition, the diode ideality factor n affects the slope of I-V curve near the maximum power point. Typical values for n are between 1 and 2 and 1.02 used in this research which was obtained by matching the shape of the manufacturer's I-V curves.

2.1.2 Piecewise Linear Model

The second model is the piecewise linear (PWL) "4-diode" model that allows fast simulation. This is a good trade-off in terms of diode number in the model. The more diode are used the smoother I-V curve is obtained. However the complexity of the model and the simulation duration are increased significantly.

As shown in the equivalent circuit diagram, the model is based on ideal zener diodes which have fixed voltage drops and it is fed by a constant-current source which is equal to I_{SC} . The single diode D_4 has a voltage drop of V_{OC} . R_S and R_P are included in this model. Adjusting the voltage drops and the resistances (the series resistances to the diodes) the vertex points of the I-V curve are simply readjusted in order to match with

the experimental results of a given PV module. Parameters' specifications of the 4-diode circuit based on the PV module BP380U under nominal conditions are given in Table 2.3. The irradiance effect is illustrated with I-V and P-V curves that are created with PWL model as seen in Table 2.2. Consequently, PWL model is used in the following chapters for the proposed grid-connected current-source inverter topology.

2.1.3 Rectangular Model

As it can be seen in Table 2.2 the ideal solar cell I-V curve has a characteristic that approaches a rectangle. The model is based on a constant-current source and a single zener diode. The rectangular model uses the values at MPP for the short-circuit current and the zener diode voltage drop. Table 2.3 also provides the model specifications at the rectangular model of the module BP380U under nominal conditions. Using this model also allows fast simulation. Despite its limited accuracy compared to other two models, this model will be used for the performance characteristics of the ideal CSI in Chapter 4.

2.1.4 Irradiance and Temperature Curves with Normalisations

Table 2.4 is given to show the non-linear model predictions for the BP380U I-V and P-V curves for irradiance and temperature variations. The first row in the table shows the actual values where the MPP are shown with circles. The second row corresponds to the normalised values of the first row reference to the MPP under nominal conditions (1000 W/m^2 , 25°C), which is followed by the normalised plots at MPPs.

Fig. 2.2 shows the effect of irradiance and temperature variation on the PV module output voltage V_0 at the maximum power point. The irradiance effect is given in Fig. 2.2(a). As shown in Fig. 2.2(b) since the voltage remains relatively constant except at low values of irradiation, V_0 decreases significantly with temperature.

As marked in the normalised I-V curve in Table 2.4 there is 0.37 pu voltage difference between -25° and 75°C . This has a large impact on the output power (almost 35%). These normalised values are used to identify desirable input voltage MPP tracking range to design power converter in Chapter 4.

TABLE 2.4: Effect of different normalisations on the I-V and P-V curves of the BP380U module under irradiance and temperature changes. First row: actual curves. Second row : all curves are normalised to MPP under nominal conditions. Third row: each curve is normalised to its own MPP. The circles represent the MPP.

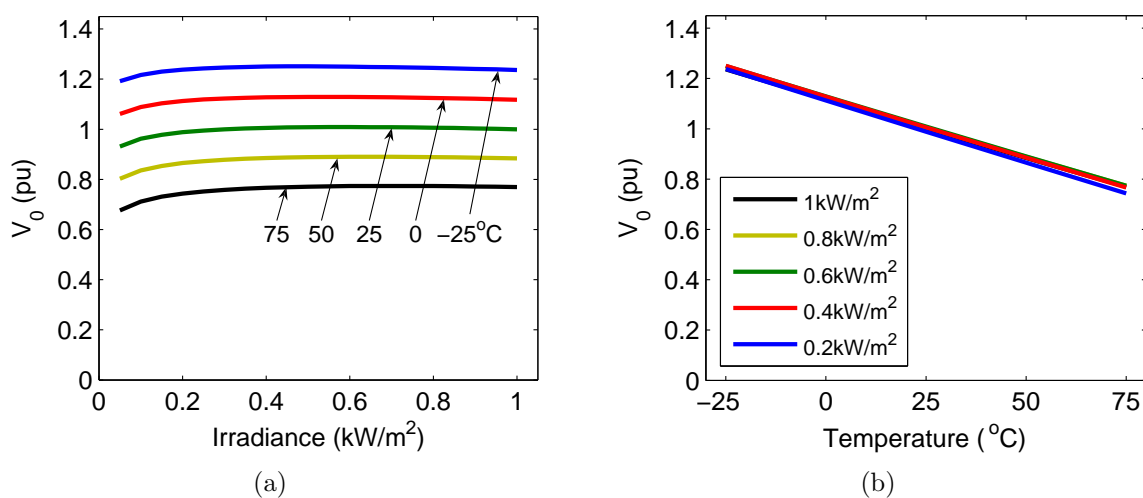
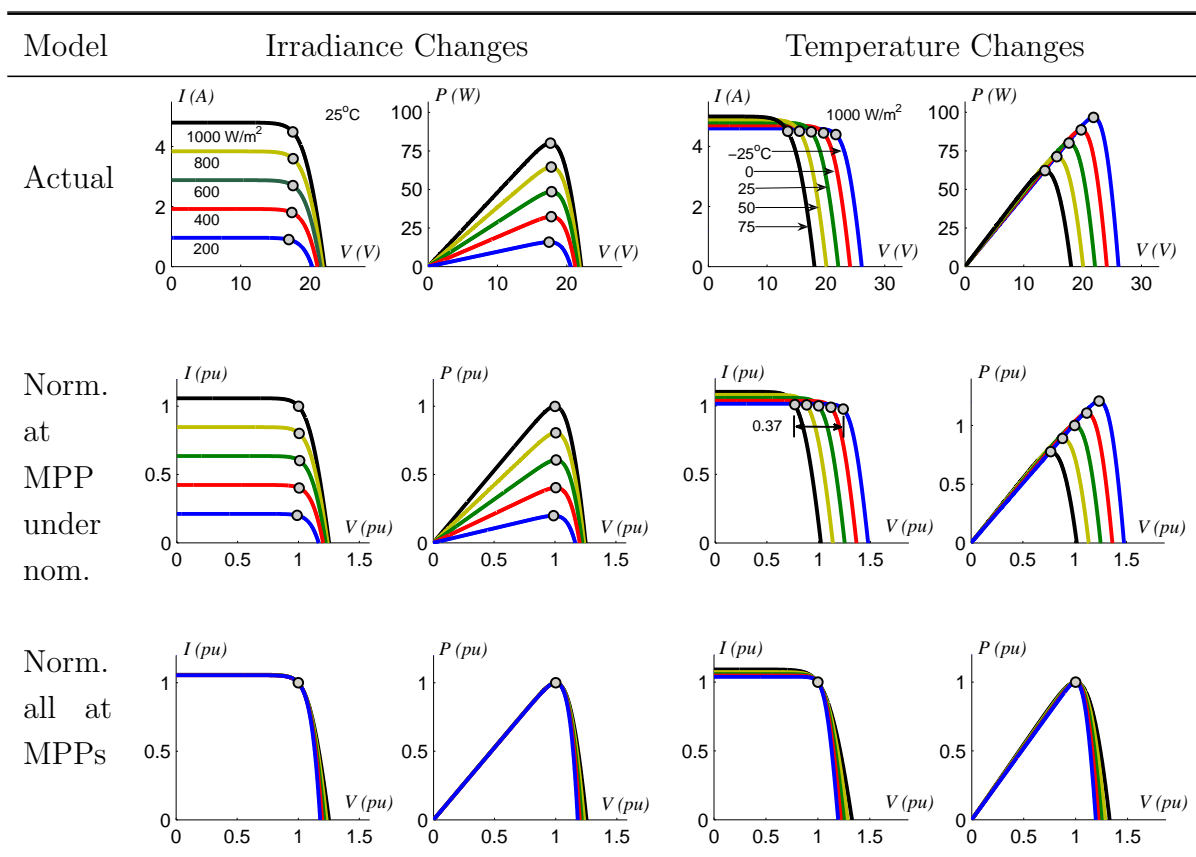


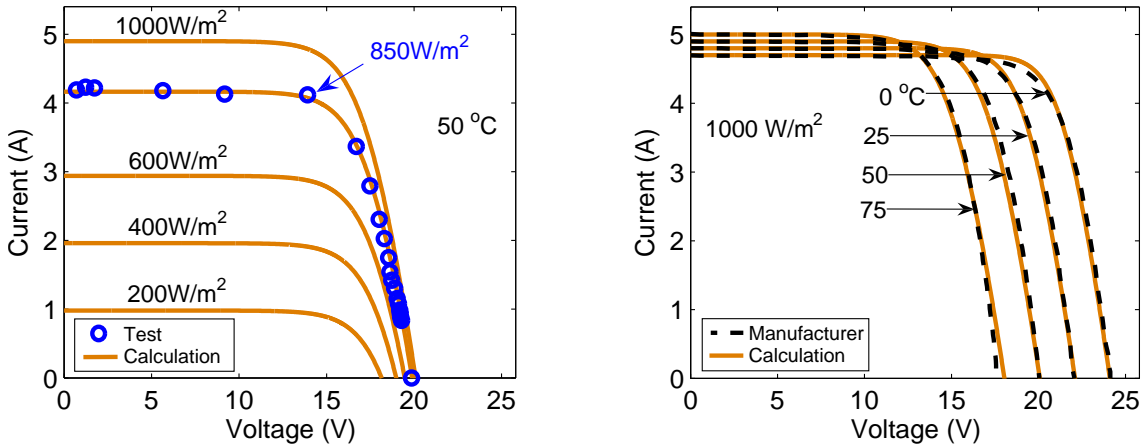
FIGURE 2.2: Voltage variations, reference to (a) irradiance and (b) temperature at MPP.

As illustrated the third row of the Table 2.4 shows the curves which are normalised based on its own MPP value. It is clearly seen that the normalised shapes of the current-voltage and power-voltage curves are largely unaffected by the temperature and the irradiation variations. These normalised values of the I-V and P-V curves are used in Chapter 3 to calculate the average output power reduction of PV arrays due to the single-phase output power.

2.2 Experimental Testing

The BP380U PV module was tested outdoors using sunlight. The irradiation and temperature levels were unknown during the tests. The measured results are compared with the non-linear model calculations in Fig. 2.3(a) for various irradiation levels by using the parameter specifications of the BP380U PV module. It was found that an 850 W/m² irradiance level and a 50°C cell temperature resulted in a good agreement with the experimental results.

The non-linear model calculations are shown for various temperatures in Fig. 2.3(b). They are compared to the manufacturer’s data, and show an excellent correspondence.



(a) Non-linear model I-V curves for different irradiance levels including the test data

(b) Non-linear model and manufacturer’s I-V curves for different temperatures

FIGURE 2.3: Non-linear I-V curves for various irradiance and temperature values including (a) outside test results and (b) manufacturer’ data sheet values.

2.2.1 Dark I-V method

The dark current-voltage (dark I-V) measurement method is also commonly used to investigate the performance characteristics of solar cells [26]. The dark I-V test circuit is given in Fig. 2.4(a) and block diagram which is connected to the CSI is shown in Fig. 2.4(b). The constant-current source of the dark I-V arrangement is set to an I_{SC} value which corresponds to 1000 W/m^2 irradiance value. It involves covering the PV module (to eliminate the light-induced current) and using an external constant-current source (CCS) to simulate the light-induced current. This is convenient as the testing can be performed indoors and the irradiance level can be easily controlled and kept constant during the test. However the temperature of the PV modules may not be realistic as PV modules often operate at much hotter temperatures than 25°C except in cold climates.

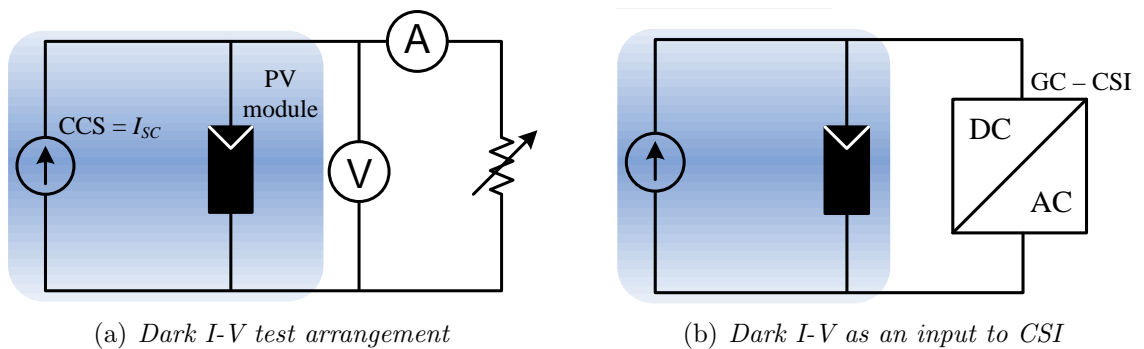


FIGURE 2.4: (a) *Dark I-V test arrangement block diagram*, (b) *dark I-V implementation block diagram with GC-CSI*.

A comparison between the dark I-V method measurements and the non-linear model calculations is provided in Fig. 2.5. Two PV modules are connected in series to obtain a PV array for the CSI application. As the temperature of the PV modules was not measured, two different temperature values (15°C and 25°C) were simulated with the non-linear model. Although neither curve matches the dark I-V test results perfectly, the 25°C curve shows a better match near the MPP.

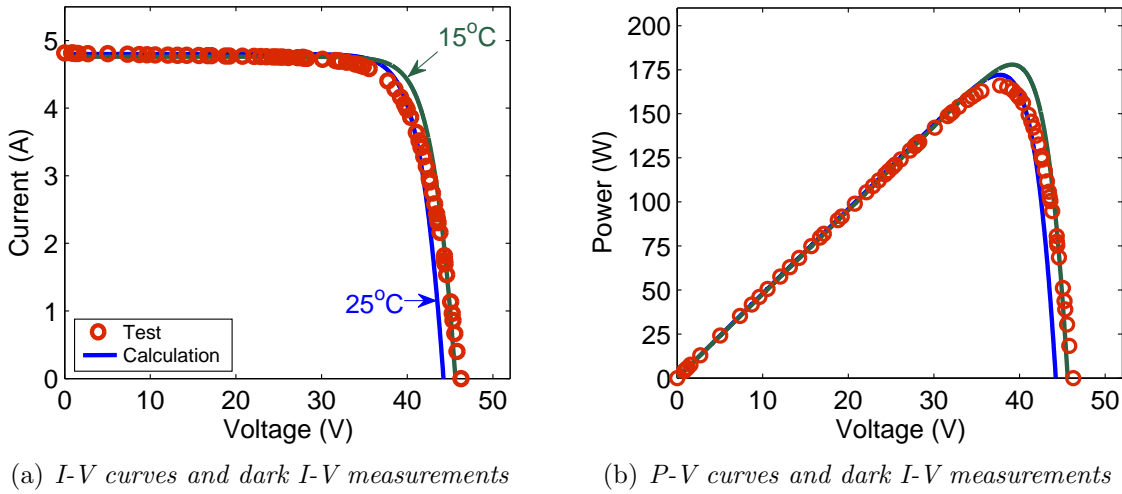


FIGURE 2.5: The non-linear model (a) I - V and (b) P - V curves for 15° and 25° C temperature values including dark I - V results at 1000 W/m^2 irradiance.

2.3 Conclusions

This chapter described three different PV cell models which are aimed to be used in the research to investigate the grid-connected current-source inverter simulations. Non-linear, 4-diode and rectangular PV cell models were explained.

It was shown that 4-diode model can provide highly accurate model while offering fast calculations for computer simulations. Normalisations of these models were also introduced. The normalisations that are based on nominal conditions will be used for input voltage determination of the CSI in Chapter 4. The non-linear model normalisations which were individually normalised will be used for power loss analysis in Chapter 3.

The non-linear model provided in this chapter was verified with the outdoor measurements and manufacturer's data. The dark I - V test arrangement was also explained and verified with the non-linear model. To provide an easy access and flexible test arrangement the dark I - V method will be used in Chapter 6 for testing the grid-connected current-source inverter prototypes.

CHAPTER 3

ENERGY STORAGE

It is important to identify and analyse the relationship between the average output power reduction of PV array and the array voltage and current ripple. Therefore, this chapter provides the relationship between the PV array output ripple and the DC link energy storage for single-phase grid-connected inverters. The balanced ripple definition, which compared with the common centred ripple definition, is introduced in the chapter and a number of examples are given to show how the results can be applied to practical designs.

3.1 Energy Storage Requirement

The output power of a single-phase inverter fluctuates at twice the line frequency (i.e. 100 Hz for a 50 Hz supply). Since the inverter output stage does not have any internal energy storage component, these fluctuations are also seen in the input of the inverter. Due to the characteristics of the PV array it is necessary to keep the instantaneous PV array output power as constant as possible to maximise the average PV output power. Thus single-phase GC inverters use an energy storage element between the output of the PV array (DC link) and the input to the inverter power stage to maintain the instantaneous power fluctuations seen by the PV array at an acceptable level. Ideally

the power fluctuations should be zero that requires an infinitely large and lossless energy storage element. However, in practice this is not possible which causes reduced PV array output power. Fig. 3.1 shows the block diagram which provides initial understanding of the power reduction process.

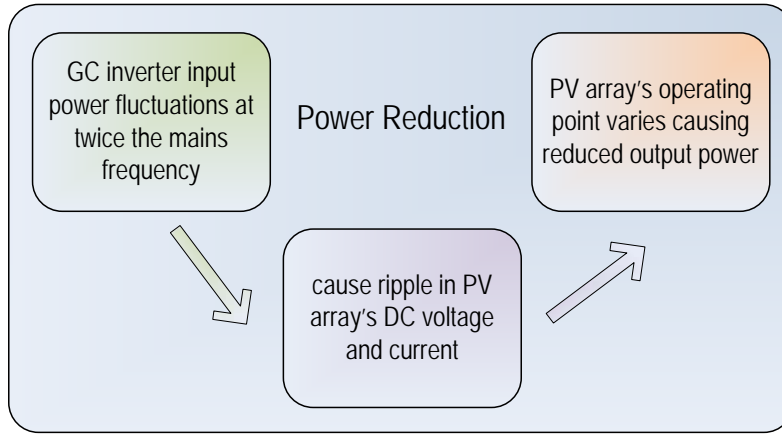


FIGURE 3.1: Block diagram of the power reduction.

In addition the inverter pulse-width modulation (PWM) control causes the inverter input and output power to fluctuate at the PWM switching frequency. In general, because of the lower frequency of the 100 Hz ripple, it dominates over the PWM ripple effect.

As it is well known, GC inverters can be classified as voltage-source inverters (VSI) which use a DC link capacitor, and current-source inverters (CSI) which use a DC link inductor. Figs. 3.2(a) and 3.2(b) show such single-stage VSI and CSI topologies. The input DC link energy storage element is used to store energy for both the 100 Hz and PWM frequency components.

It is desirable to minimise the required amount of DC link energy storage due to its cost, size and weight, and also due to concerns about its reliability (particularly for electrolytic capacitors). The minimum amount of DC link energy storage is set by two limitations:

- the maximum allowable PV output voltage or current ripple to limit the average PV output power reduction to a reasonable level, and
- the maximum allowable inverter input voltage ripple (for VSI) or current ripple (for CSI) before unacceptable levels of distortion are produced in the inverter output current being fed into the grid.

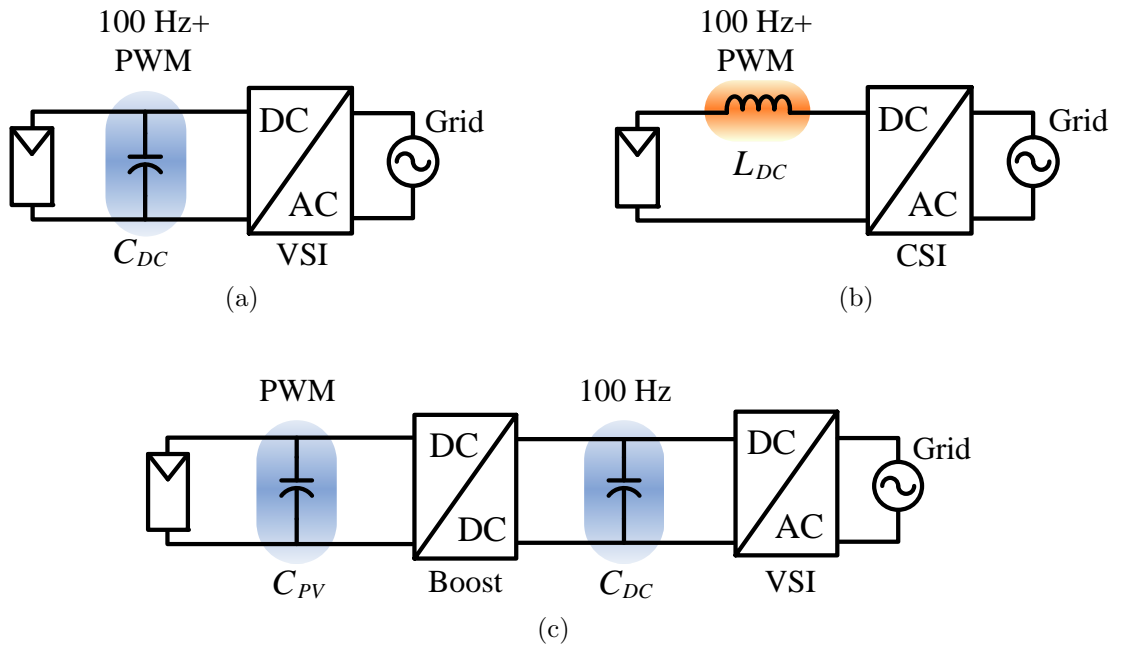


FIGURE 3.2: Common single-phase PV inverter topologies as (a) VSI, (b) CSI and (c) two-stage VSI.

A method for separating these two limitations is to use a two-stage VSI converter topology as shown in Fig. 3.2(c). This consists of adding a DC/DC converter before the VSI. In this circuit, the DC/DC converter isolates the PV array from the 100 Hz ripple component and performs the MPP tracking. The PV array output capacitor (C_{PV}) only needs to be sufficiently large to filter out the power variations associated with the PWM switching. The DC link capacitor (C_{DC}), at the input of the inverter, now provides the 100 Hz ripple energy storage. The size of this capacitor can thus be set without concern for its effect on the PV array output power. However, the disadvantages of the two-stage topology are reduced efficiency and increased cost.

Therefore this study will focus on single-stage converters. In these converters choosing the amount of energy storage is a trade-off. Increasing the amount of energy storage minimises the PV array output power reduction but increases the cost and losses in the energy storage element. This is more of an issue with CSI due to the higher losses in DC link inductor compared to the a DC link capacitor with the same energy storage capacity.

This chapter will provide a systematic approach to analyse and optimise the energy storage requirement for the single-phase GC inverters. The chapter is organised as follows.

In Section 3.2 the relationship between the amount of DC link energy storage and the inverter input voltage and current ripple is discussed. In Section 3.3 the PV array average power reduction calculations are explained. In Section 3.4 existing PV inverter design examples are discussed. A summary of the results is also provided in the final section of this chapter.

3.2 Current/Voltage Ripple Calculation

Grid-connected CSIs are designed to feed sinusoidal current into the grid at unity power factor. Fig. 3.3 shows the PV array ripple current, the instantaneous inverter input voltage, input power and the output power waveforms for ideal and practical cases. Since the inverter has no internal energy storage elements, the instantaneous inverter input power and output power must be the same assuming an ideal (lossless) inverter. As it can be seen in the figure, the average power generated by the PV array (dashed line) is ideally the same as the average power fed into the grid. Therefore, the difference between the instantaneous power required by the inverter and that supplied by the PV array should be provided by stored energy in the DC link inductor. This stored energy depends on the current and thus the inductor current and hence the PV array current shows ripple. This ripple results in a reduction in the average output power of the PV array.

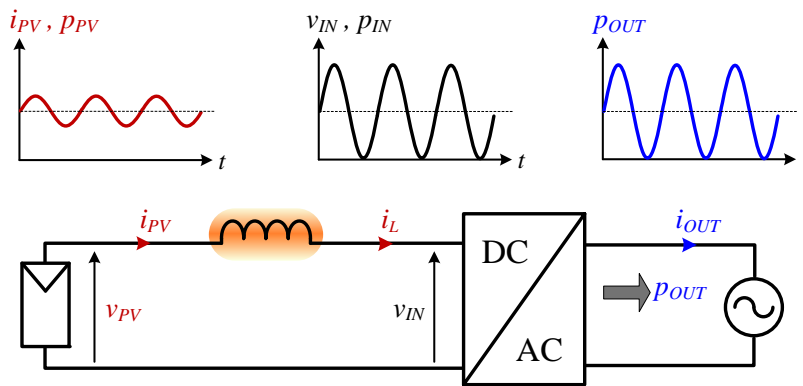


FIGURE 3.3: Single-phase current-source GCI showing the PV array, the DC link inductor, inverter, power grid and idealised current, voltage and power waveforms.

Though it is clear that the issue of average power reduction of PV arrays due to output voltage or current ripple is widely recognised and taken into account in practical designs,

there appears to be limited analysis of this effect in the literature. Therefore in this section of the thesis, the effect of the energy storage element on current and voltage waveforms will be studied systematically for power reduction estimation.

The main reference identified in the literature was the work done by Kjaer [30] in examining the effect of voltage ripple on a single-stage VSI inverter for both standard silicon and cadmium-telluride (CdTe) PV arrays. Kjaer assumed the voltage ripple was sinusoidal and centred around the optimum voltage. He modelled the theoretical PV array power versus voltage characteristics around the MPP voltage and used this to determine the allowable voltage ripple for average power reductions ranging from 0.1% to 2%. Kjaer also analysed the relationship between the capacitor size and the voltage ripple produced by the 100 Hz instantaneous power fluctuation and developed a relationship between the minimum required capacitor size and the PV array parameters and allowable average power reduction.

Casadei et al. [31] used the voltage ripple for MPP tracking. They showed for a VSI that the voltage ripple was a function of average output power P_0 , grid angular frequency ω and DC link capacitance C_{DC} :

$$\frac{P_0}{\omega} = C_{DC} (V_{dcMAX}^2 - V_{dcMIN}^2) \quad (3.1)$$

Ninad et al. also employed the same definition to predict DC link capacitor value [32].

In the following section the energy buffering concept will be explained schematically to obtain a simple relationship between the current (and voltage) ripple, the output power and the stored energy.

3.2.1 Effect of Energy Storage on Current/Voltage

In the analysis of current ripple it will initially be assumed that the inverter is operating with 100% modulation index and that the inductor current $i_L(t)$ is essentially constant. The inverter input voltage $v_{IN}(t)$ is given by :

$$v_{IN}(t) = \frac{p_{OUT}(t)}{i_L(t)} \quad (3.2)$$

In addition as it is illustrated in Fig. 3.3, it will initially be assumed that the PV array output voltage v_{PV} , current i_{PV} and hence output power are constant. As the inductor acts as a short circuit to DC, v_{PV} has a value that is equal to the average value of $v_{IN}(t)$. Although it is assumed that the output power of the solar array is constant, the instantaneous input power of the inverter is time-varying. The DC link inductor supplies or absorbs the difference in instantaneous power between the PV array output power and the time-varying inverter input power. Fig. 3.4 shows that the stored energy in the inductor has an average value of E_0 and a ripple of ΔE . The energy stored in the inductor varies as a function of current and so the inductor current $i_L(t)$ must change during the course of the cycle as energy is absorbed and released. Considering the voltages, it can be seen that the inductor voltage is equal to the difference between the solar array voltage v_{PV} and the inverter input voltage v_{IN} , and is hence a sine wave with zero mean. The inductor current is thus a cosine waveform with an average value of I_0 which is equal to the mean PV array current.

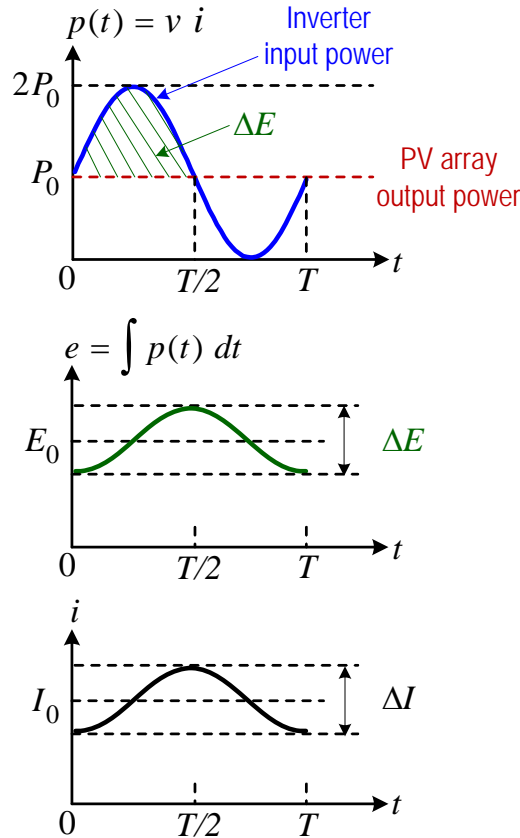


FIGURE 3.4: Demonstration of energy buffering which shows the relation between the instantaneous power flow, the energy stored in the inductor and the inductor current ripple.

The average energy E_0 stored in the DC link inductor L is given by :

$$E_0 = \frac{1}{2} L I_0^2 \quad (3.3)$$

The inductor energy ripple ΔE is :

$$\Delta E = \int_0^{T/2} V_0 I_0 \sin(\omega t) dt = \frac{1}{\pi} V_0 I_0 T \quad (3.4)$$

where T is the period of the instantaneous power waveform (100 Hz), V_0 is the DC voltage at the MPP and ω is the angular frequency of the grid voltage. For small values of ripple, it can be shown that the current ripple ΔI can be related to the energy ripple ΔE as :

$$\frac{dE}{di} = L i \quad \Rightarrow \quad \Delta E = L i \Delta i = L I_0 \Delta i = \frac{1}{\pi} P_0 T \quad (3.5)$$

The above equation can be re-arranged for the current as :

$$\frac{\Delta i}{I_0} = \frac{\Delta E}{2 E_0} = \frac{P_0}{2 \omega E_0} \quad (3.6)$$

and for a VSI with a DC link capacitor as :

$$\frac{\Delta v}{V_0} = \frac{\Delta E}{2 E_0} = \frac{P_0}{2 \omega E_0} \quad (3.7)$$

Thus a simple relationship can be given between the current (and voltage) ripple and the output power and the stored energy E_0 .

3.3 PV Power Loss Calculations

The 100 Hz current and voltage variations result in a reduction in the average output power of the PV array although the average PV current may still be the current at the maximum power point (I_0) as shown in Fig. 3.5. This is because the maximum power only occurs when the current is at I_0 so any variation causes a reduction in the PV array output power. The power reduction associated with PV array current ripple cannot be compensated by MPP tracking algorithms. These algorithms slowly adjust the average

PV output voltage (or current) in order to maximise the array output power, despite variations in either irradiance or temperature, and have no effect on the 100 Hz ripple.

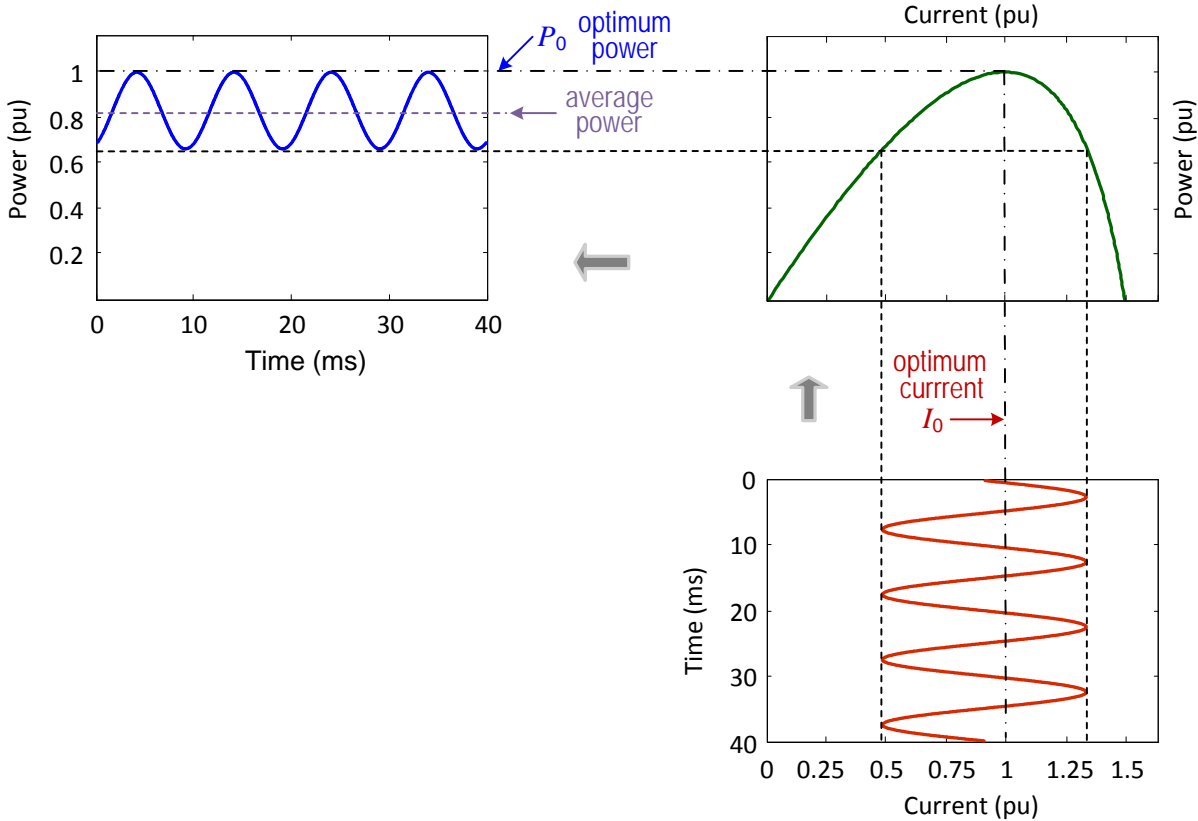


FIGURE 3.5: PV array output current variations cause a reduction in the average PV array output power, for a CSI.

3.3.1 PV characteristics

The shape of P-I and P-V curves near MPP is critical to find power loss due to the inverter's input power fluctuations. Fig. 3.6 shows normalised power-current curves based on two series-connected 80 W PV modules (BP380U). These curves are generated by using normalisation procedure described in Chapter 2. It is important to notice that the MPP is the same for each individually normalised curve. This implies that the shape of P-I curve is relatively independent of irradiance and temperature. The following calculations were thus done using the normalised curves under nominal conditions (1000 W/m² and 25°C).

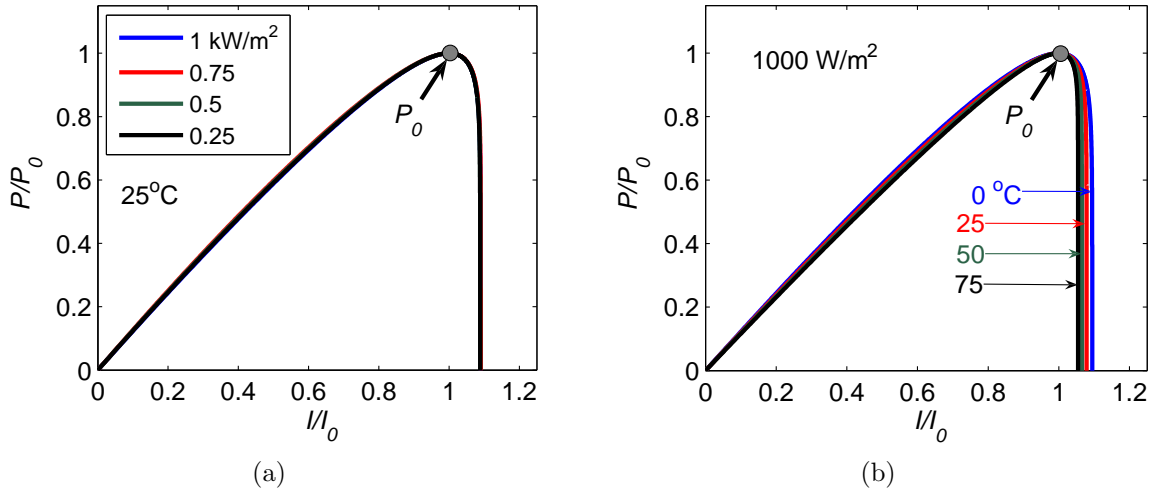


FIGURE 3.6: Normalised power-current curves for varying (a) solar irradiance at 25°C and (b) module temperature at 1000 W/m².

3.3.2 Average Power Reduction

Fig. 3.7 provides two different approaches for defining the peak to peak current ripple (ΔI). Fig. 3.7(a) shows the definition used by Kjaer [30] where the ripple is “centred” on the MPP current I_0 . This used a second-order Taylor series approximation for the PV array power versus voltage characteristic. An alternative definition proposed in this paper is the “balanced” approach shown in Fig. 3.7(b). This definition makes the output power equal at the current extremes. The centred definition gives a reasonable approximation at small values of ripple (see Fig. 3.8), however the balanced definition provides greater output power and so more accurately represents the operating point that is tracked by the MPP algorithm.

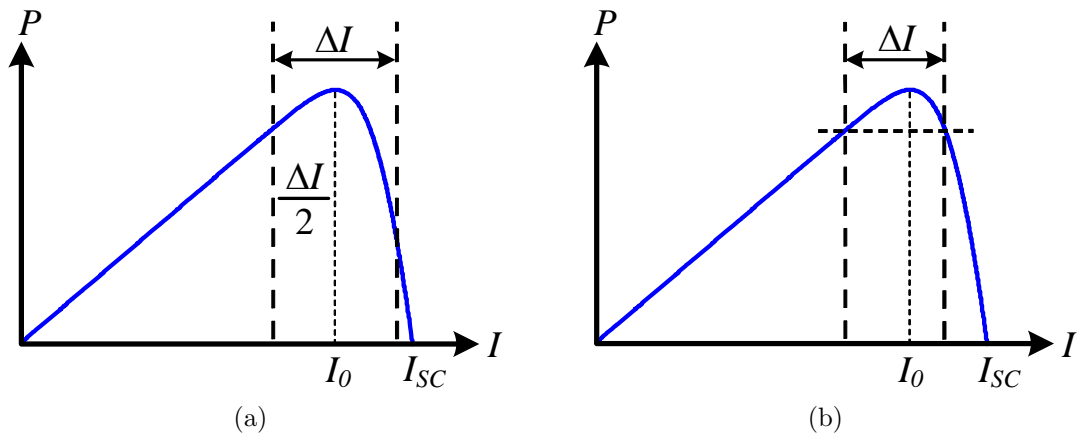


FIGURE 3.7: Definition of centred (a) and balanced assumptions (b) for ΔI .

Fig. 3.8 compares the average power reduction due to voltage or current ripple for both the centred and the balanced method. This figure is based on the normalised power-current and power-voltage curves under nominal conditions, and the two ripple definitions. The values were found by assuming a sinusoidally time-varying voltage or current ripple (see Fig. 3.5) and then calculate the resultant instantaneous output power waveform, and hence the average power reduction. The curves for the balanced voltage ripple and balanced current ripple are nearly identical. The centred ripple definition gives higher values of power reduction, particularly for the centred current ripple case at higher ripple magnitudes. Both balanced and centred definitions give similar results for small values of ripple but they diverge as the ripple increases; e.g. a 12% current ripple yields a 2.1% power reduction using the centred definition, however the balanced definition yields only 1.3%. For comparison purposes, the calculated results from [30] based on the centred voltage-ripple definition are also shown in Fig. 3.8 as circles. It shows a good correspondence with the centred voltage ripple result at low values of ripple, but diverges significantly at higher ripple values due to the Taylor series approximation to the P-V curve.

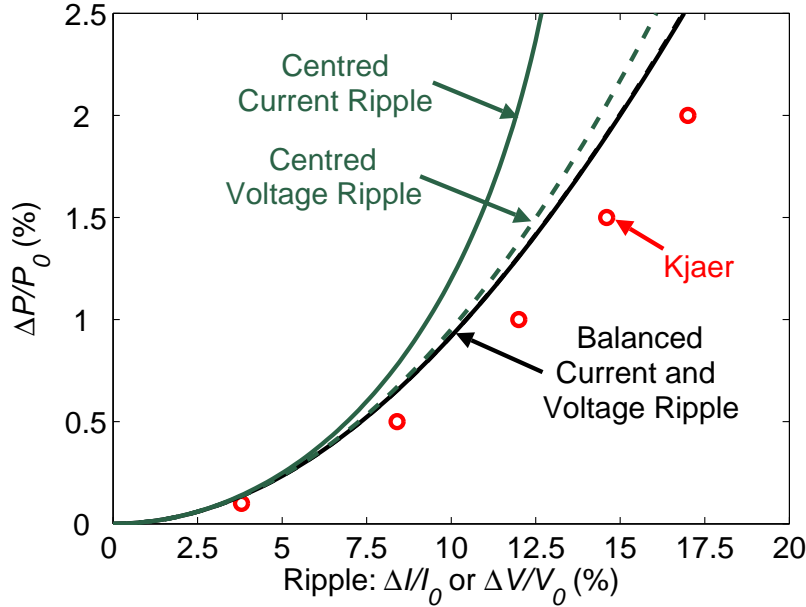


FIGURE 3.8: Average power reduction versus voltage ripple (dashed lines) and current ripple (solid lines) using both centered and balanced ripple definitions. The centered voltage ripple results from Kjaer [30] are shown as circles.

3.4 Application Examples

Table 3.1 examines four existing grid-connected VSI and CSI designs and provides data on the grid frequency, rated PV array output power, rated maximum current and voltages, DC link capacitor value, DC link inductor value, energy storage values as mJ/W, PV array power reduction and energy storage component resistance loss. The peak to peak ripple values (ΔV for VSI and ΔI for CSI) are calculated using (3.6) and (3.7). Then the ripple calculation leads to predict PV array power reduction $\Delta P/P_0$ from Fig. 3.8 in respect to balanced definition.

TABLE 3.1: *Grid-connected PV VSI and CSI design examples based on balanced method. Power loss due to DC link element (resistance) PV array power reduction and total loss are given.*

	VSI		CSI	
	[33]	[34]	[16]	[19]
Reference				
Grid frequency	50 Hz	60 Hz	60 Hz	60 Hz
Rated max. input power P_0	138 W	600 W	225 W	408 W
Capacitance	6.8 mF	3 mF	-	-
Inductance	-	-	200 mH	400 mH
Input current for P_0 (I_0)	3.15 A	4.4 A	5.7 A	6.15 A
Input voltage for P_0 (V_0)	43.8 V	136.3 V	45 V	66.3 V
Energy storage per W.	47.3 mJ	46.4 mJ	14.4 mJ	18.5 mJ
Ripple	0.7 V	3.82 V	0.6 A	0.44 A
Ripple (%)	1.6	2.8	10.6	7.1
PV array power reduction $\Delta P/P_0$ (%)	0.04	0.05	1	0.86
Capacitor ESR	13 m Ω	14 m Ω	-	-
Inductor resistance	-	-	1.3 Ω	-
$I^2 R$ loss P_R/P_0 (%)	0.09	0.05	16	-
Total Power loss (%)	0.13	0.1	17	-

Both VSI designs yield $<0.1\%$ PV array average power reduction. The obtained total power reduction is less than 0.2% . The VSI design energy storage does not cause considerable loss and DC link capacitors are inexpensive. As seen from the CSI design results, the copper resistance causes significant amount of loss. This is the biggest concern in terms of efficiency of the CSIs. To reduce the inductor loss the DC link inductor can be decreased in size. However, the size decrease raises the PV array power reduction. Both CSI designs used relatively high inductances hence require large DC link inductor.

However, in Table 3.1 the energy storage values are lower compare to VSI design. Consequently the trade-off between the size of the inductor and the PV array average power reduction must be analysed. The analysis of an optimised DC link inductor to minimise the total system loss is explained in Appendix A. Please note that the DC link capacitor equivalent series resistance (ESR) values are obtained from a standard electrolytic capacitor data sheet in [35].

3.5 Summary

This chapter has investigated the relationship between the amount of energy storage in grid-connected PV inverters and the average power loss due to the PV array voltage and current ripple. The key results are :

- there is a simple relationship between the PV array voltage or current ripple in voltage and current source inverters, and the output power and the amount of stored energy required;
- the shape of the normalised PV array power-voltage and power-current curves are not sensitive to irradiance or temperature variations;
- the definition of “balanced” current (or voltage) ripple based on equal power reduction at the extreme values gives more realistic estimates of PV output power reduction than assuming the ripple is centered on the optimum value;
- using the balanced definition, the average power reduction versus ripple magnitude is very similar for both voltage and current ripple;
- there is a trade-off between the inductor (or capacitor) size and the PV average power reduction.

CHAPTER 4

FUNDAMENTAL ANALYSIS

Chapter four describes the idea, operating principles and features of a single-phase low-cost current-source grid-connected inverter. In the chapter, the proposed concept and its components are discussed. The determination of input voltage is provided. The ideal grid-connected current-source inverter is introduced and simulated. This is achieved by assumptions that all device losses, pulse-width modulation (PWM) switching effects, and output filter resonance effects are ignored. In addition, the baseline parameters are introduced. In the simulation studies, the rectangular and 4-diode PV array models are used as explained in Chapter 2. The effect of modulation index (m_A), energy storage (E) and irradiance (G) variations are also analysed. Finally, total harmonic distortion (THD) and power factor (PF) are examined so as to meet Australian Standards [9].

4.1 Proposed Concept

A current-source inverter topology for a small-scale grid-connected wind power and PV applications are shown in Fig. 4.1. The wind power application is based on high-inductance three-phase permanent magnet (PM) generator which acts as an AC constant

current-source, where an uncontrolled bridge rectifier produces DC output current. However it has six-times fundamental frequency ripple varying with the PM generator speed which affects the low-pass filter design in respect to PM generator speed.

The proposed grid-connected inverter is based on a current-source input similar to the wind application. In this thesis, the constant current-source is obtained using a PV array with a DC link inductor. A block diagram of the proposed inverter is shown in Fig. 4.1, along with the expected input and output currents of the four inverter stages, i.e. the constant-current source, the waveshaper (WS), unfolding circuit (UC), and low-pass filter. The inverter operates from an essentially constant input current, delivered by the PV modules through the DC link inductor. The current waveshaper and unfolding circuit stages are used to produce a unipolar PWM current, which is filtered and fed to the grid, via the low-pass filter.

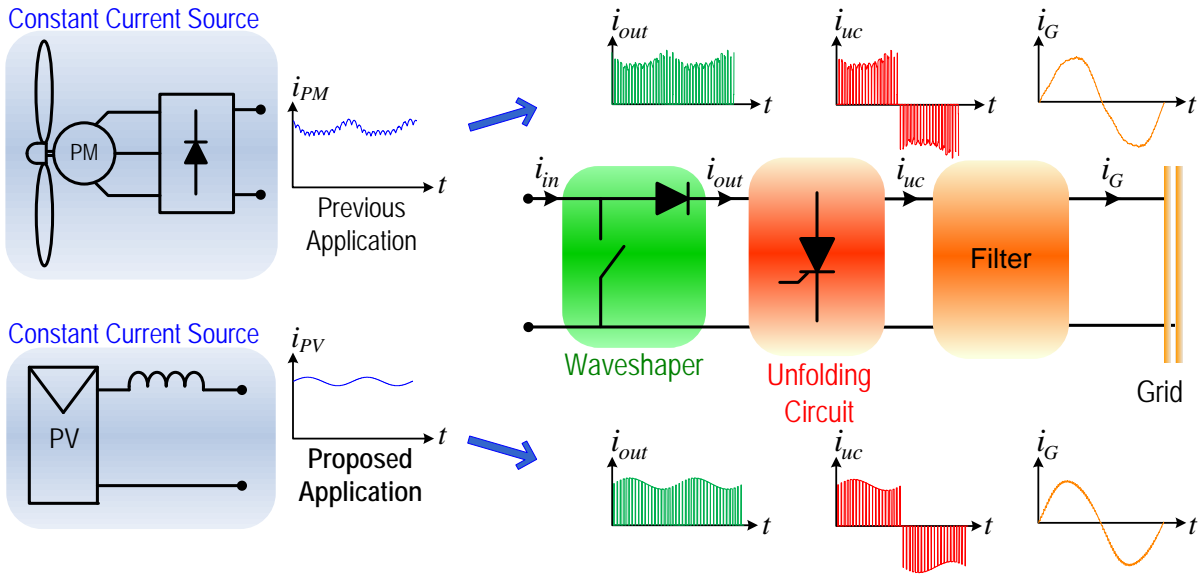


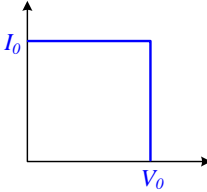
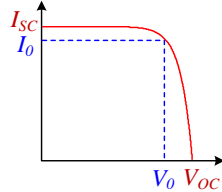

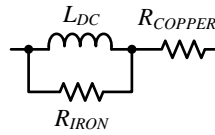
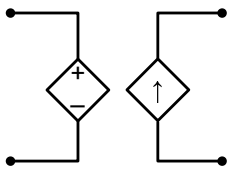
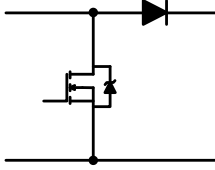
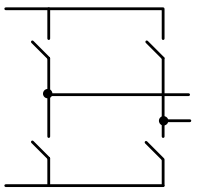
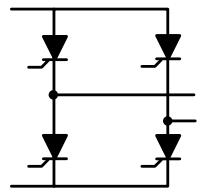
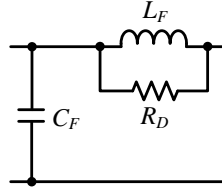
FIGURE 4.1: Grid-connected CSI topology showing previous wind and proposed PV applications constant-current inputs, and the current waveforms for each stage.

Both the wind application and the proposed PV applications have PWM and 100 Hz ripple in a 50 Hz AC grid. The large amplitude PWM (high) frequency ripple can be attenuated by using a low-pass filter to meet the grid requirements [9]. The 100 Hz ripple due to the single-phase, 50 Hz output causes the PM generator to vibrate and the PV array current to fluctuate. The PM machine output power is not significantly affected except by a possible slight reduction in generator efficiency. However the 100 Hz ripple can cause the maximum output power (MPP) from the PV array reduced.

4.2 Ideal Current-Source Grid-Connected Inverter

Table 4.1 illustrates the components of the grid-connected current-source inverter and shows both ideal and non-ideal models. The ideal component models ignore losses such as DC link inductor model which has no copper and iron (hysteresis and eddy current) losses or switches without on resistance and switching losses. The high-frequency switch WS is essentially a high-speed switch and a reverse-blocking diode. However in the ideal model the output current (4.1) and voltage (4.2) relationships are used with two controlled sources to realize the WS switch. This allows the elimination of PWM switching effects and hence the CSI can produce a sinusoidal output without the need for a low-pass line filter.

TABLE 4.1: Ideal and non-ideal components of the proposed inverter.

Component	Ideal	Non-Ideal
PV array		
DC link inductor		
Waveshaper		
Unfolding circuit		
Low-pass filter	Low-pass filter is not required	

$$i_{OUT} = i_{IN} (1 - d) \quad (4.1)$$

$$v_{IN} = v_{OUT} (1 - d) \quad (4.2)$$

The circuit, along with the ideal input and output currents, are shown in Fig. 4.2. The output current i_{OUT} is the complement of the PWM duty-cycle (control signal) d as shown by (4.1), where i_{IN} is the input current.

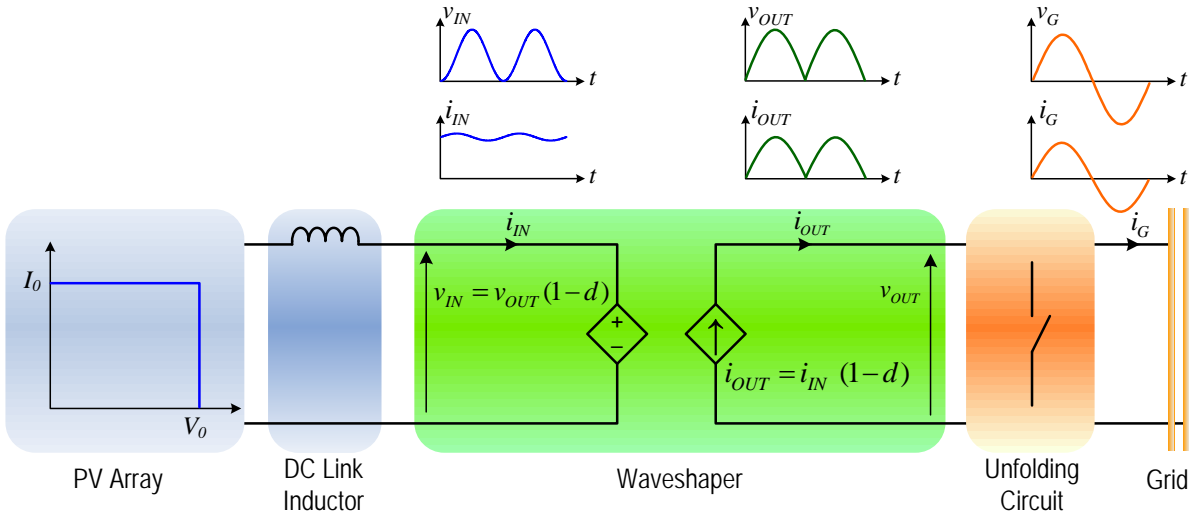


FIGURE 4.2: Ideal single-phase current-source grid-connected inverter equivalent circuit diagram.

As shown in Fig. 4.2 to model the ideal WS, a controlled voltage-source and current-source are used. The controlled current-source sets the WS output current as the product of the input current and $(1 - d)$. Equation (4.3) shows how the duty cycle of the switch is related to the modulation index m_A ,

$$1 - d = m_A |\sin \theta| \quad (4.3)$$

Likewise the controlled voltage-source sets the input voltage v_{IN} as the product of the output voltage v_{OUT} and $(1 - d)$. Hence a full-wave rectified DC output current is produced before the unfolding circuit without the PWM as shown in Fig. 4.1. The unfolding circuit, which is a thyristor (SCR) based H-bridge inverter (see Table 4.1), reverses the polarity of the PWM chopped DC current at twice the grid frequency to

The rectangular and 4-diode PV array models are created using the I-V characteristics of the BP380U PV module as described in Chapter 2. The rectangular model consists of a constant current-source and parallel zener diode. The voltage and current values correspond to the MPP values under nominal conditions. The 4-diode model comprises of a resistor and diode network which was designed to approximate the actual PV array I-V curve (see Chapter 2). The modulation controller is a unity amplitude sinusoidal signal which is passed through an absolute function to generate the duty-cycle command. Each pair of switches in the UC circuit are turned on at the line frequency to reverse the polarity of the input current during one half of the supply and hence produce a sinusoidal output current. Table 4.2 shows the simplified CSI simulation parameters under nominal conditions.

TABLE 4.2: *Simulation model parameters of the simplified GC CSI using rectangular and 4-diode models at the maximum power point ($m_A = 0.85$) under nominal conditions.*

Parameters	Values
Irradiance (G)	1000 W/m ²
PV array voltage (v_{PV}) V_0	37.29 V
PV array current (i_{PV}) I_0	4.277 A
DC link inductor (L)	200 mH
Modulation index (m_A)	85%
Grid (V_{pk})	87.75 V
Sinusoidal reference signal	1 V
Simulation Time	0.4 s
Total Time	2.4 s
Time Step	5 μ

4.3 Fundamental Operation of the CSI

4.3.1 Idealised Waveforms and Analysis

Fig. 4.4 shows a flow diagram of the current and voltage waveforms of the CSI starting from the grid using a rectangular model of the PV array.

Consider the grid voltage v_G is given by

$$v_G(t) = V_{PK} \sin(\omega t) \tag{4.4}$$

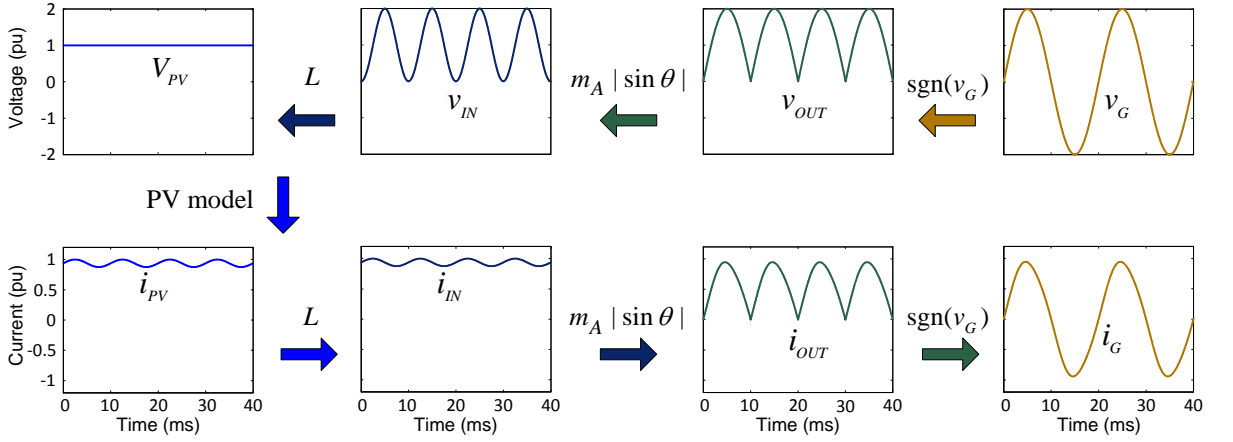


FIGURE 4.4: Ideal waveform flow diagram of the GC CSI at MPP ($m_A = 0.85$). Due to the order in the simulation study, the waveforms start from the grid voltage v_G to achieve a sinewave output current.

where, V_{PK} is the peak value of the grid voltage and ω is angular frequency of the grid. The wavershaper output voltage v_{OUT} is equal to the absolute value of the grid voltage,

$$v_{OUT} = V_{PK} |\sin(\omega t)| \quad (4.5)$$

Using the wavershaper voltage transfer equation (4.2) and the definition of the duty cycle $d(t)$ in (4.3) leads to the following expression for the wavershaper input voltage $v_{IN}(t)$,

$$v_{IN}(t) = V_{PK} m_A \sin(2\omega t) = V_{PK} m_A 0.5 [1 - \cos(2\omega t)] \quad (4.6)$$

The wavershaper input voltage is thus a double line frequency sinusoid with a DC offset. Therefore the average PV array output voltage must be equal to the average wavershaper input voltage as the DC voltage drop across the inductor is zero. Hence the average PV array output voltage v_{PV} can be given by

$$v_{PV} = \overline{v_{IN}(t)} = \frac{1}{2} V_{PK} m_A \quad (4.7)$$

The DC link inductance value and the characteristics of the PV array determine the resultant PV array output current, i_{PV} corresponding to the wavershaper input voltage in (4.7). In general this will have some double line frequency component. The wavershaper input current i_{IN} is the same as the PV array output current. The wavershaper output current, i_{OUT} , is a modulated version of the input current as given by (4.1). Finally the grid current i_G is an unfolded version of the wavershaper output current.

4.3.2 Selection of PV Array to Grid Voltage Ratio

Selection of the appropriate ratio between the nominal PV array voltage and the peak grid voltage is required for the optimal operation of the GC CSI. The MPP tracking keeps the system at the maximum power operating point by changing m_A . This tracking action occurs continually as the irradiance and/or temperature condition changes, and it requires sufficient gap around MPP. In order to provide such gap, the m_A must be under unity when the system operates at the MPP.

As it is known, the PV array temperature variations have a significant effect on the output voltage. Fig. 4.5(a) shows the simulated output power versus output voltage characteristics for the PV panel at nominal temperature (25°C), and an extreme hot (75°C) and cold (-25°C) temperature assuming nominal irradiance. Under cold conditions, the PV panel produces higher output power but requires a higher MPP output voltage (and hence a higher value of modulation index). Note that the maximum value of the modulation index is unity. If the PV array output voltage cannot be increased due to limitations on the modulation index, then the PV array output power will be less than the maximum available.

An important parameter is the choice of the modulation index under nominal temperature (and irradiance conditions) which is called the nominal modulation index. Fig. 4.5(b) shows the change in PV array output power as a function of temperature for different values of nominal modulation index. At low values of nominal modulation index, there is plenty of margin to increase the modulation index which gives the maximum output power over the widest temperature range. If the nominal modulation index is unity, then the PV array output voltage cannot be increased beyond the value under nominal conditions which results in significant power reductions under cold conditions.

It should be noted that in general the efficiency of an inverter increases with modulation index and thus there is a trade-off between the ability for tracking the MPP under cold conditions versus the inverter efficiency. Based on the results in Fig. 4.5(b) a value of nominal modulation index of 0.85 was chosen for the analysis. From (4.7) this corresponds to a voltage ratio of v_{PV}/V_{PK} of $0.85/2 = 0.425$.

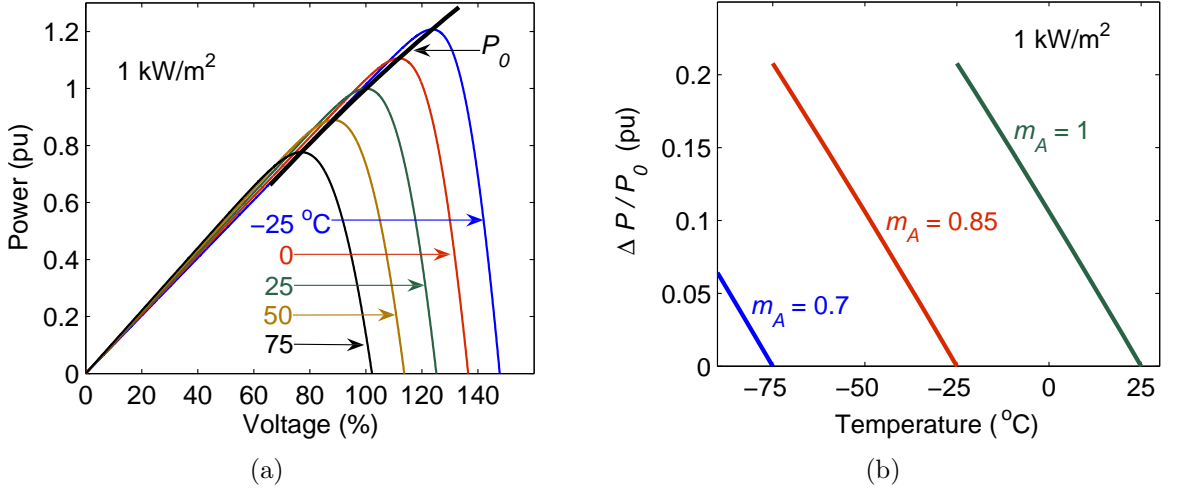


FIGURE 4.5: (a) *PV array output power variation versus PV array output voltage at MPP and (b) normalised power reduction as a function of temperature at MPP.*

4.3.3 Effect of Energy Storage

As stated previously, the selection of the amount of DC link energy storage is highly critical in GC CSIs. The amount of energy storage will be measured using the ratio of the energy E stored in the inductor to the PV array output power and is given in milli-joule per watt (mJ/W). The normalised ideal CSI current and voltage waveforms for each stage for energy storage values varying from 24 mJ/W down to 3 mJ/W are provided in Table 4.3 for a nominal m_A of 0.85.

As both the grid voltage v_G and the modulation index m_A are fixed, the WS output voltage and the WS input voltage are the same irrespective of the amount of energy storage (as shown in (4.6) and (4.7)). The PV panel I-V curve and the amount of DC link energy storage determine the resultant PV voltage v_{PV} and PV (or WS input) current i_{IN} waveforms. The value of modulation index then controls how the WS input current is converted into the grid current i_G .

Due to the single-phase inverter output, the instantaneous inverter power input fluctuates at 100 Hz. The DC link inductor acts as an energy buffer between the inverter and the PV panel and reduces the power fluctuations seen by the PV panel. As was shown in Chapter 2, these power fluctuations reduce the average output power from the PV panel and hence the power delivered to the grid.

The first column in Table 4.3 shows the I-V curve for the PV array with the trajectory of the operating locus shown as a thick line (fluctuation region). With an infinite DC link energy storage, the PV panel's output voltage and current would be DC quantities and the operating locus would be a single point on the I-V curve corresponding to the MPP. With a finite but large value of energy storage (24 mJ/W), the PV panel voltage and current fluctuations (ripple) are small however as the energy storage is reduced, the fluctuations grow in amplitude.

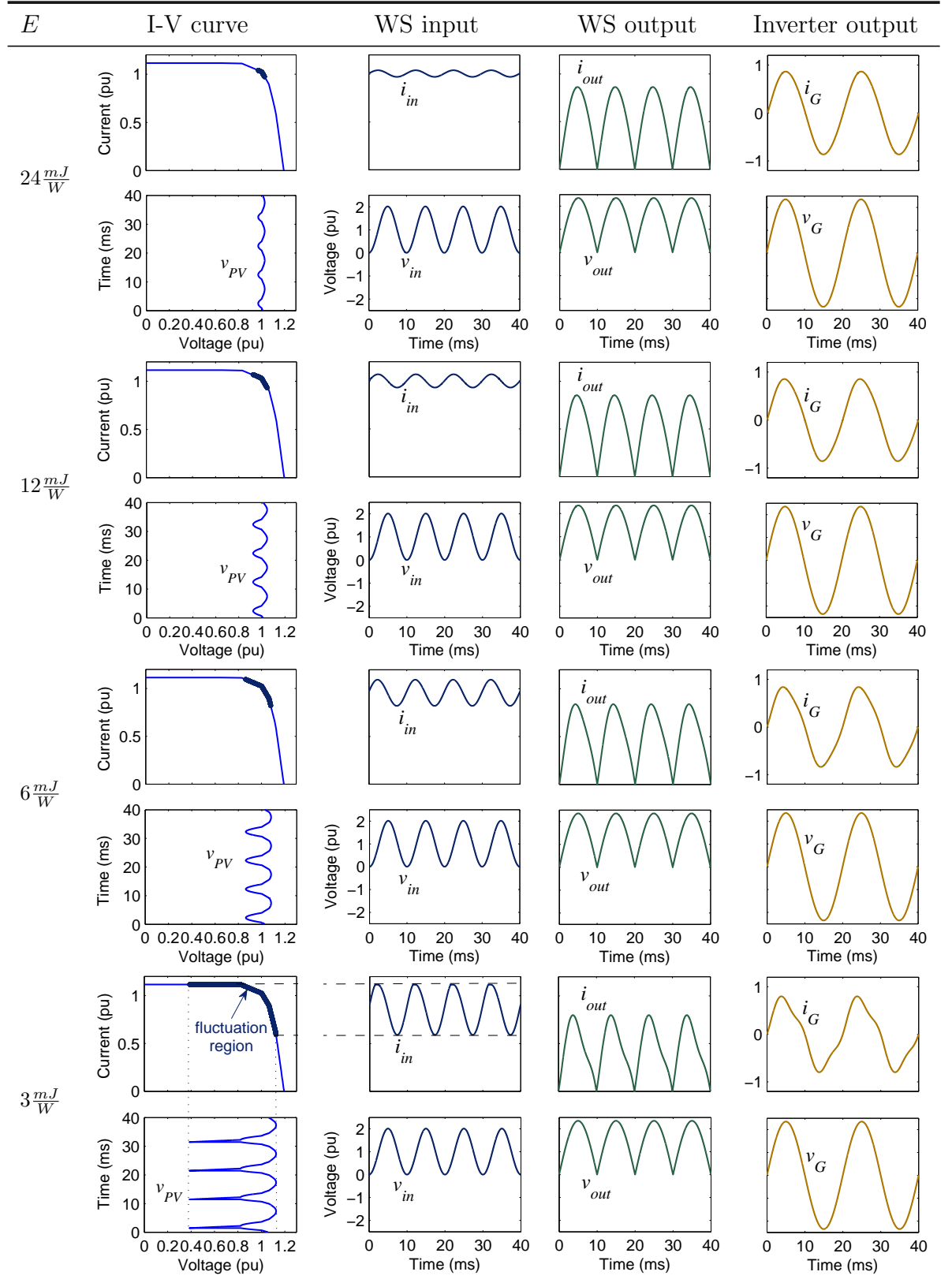
The ripple in the current represents changes in the stored energy in the DC link inductor. It is well known that in an inductor the energy is proportional to the current square (see (3.3)). The amount of input energy variation per cycle is dependent on the single-phase output power which is a constant value at rated output. As the nominal stored energy in the DC link inductor is reduced, the change in the stored energy due to the power fluctuations becomes an increasing fraction of the total stored energy and hence the current ripple increases. This is apparent in the second column of Table 4.3 where the input current i_{IN} shows a ripple amplitude which is roughly inversely proportional to the energy storage.

The input current i_{IN} is shaped by the WS switch using a sinusoidal reference waveform. If the input current is constant this produces an ideal sinusoidal grid current. The presence of ripple on the input current causes the grid current to become distorted.

Fig. 4.6(a) shows the variation of grid output power (due to the current ripple reducing the average PV output power) with the DC link energy storage. Curves are shown for three PV panel models : rectangular, 4-diode and non-linear. These are calculated using the balanced definition (see Fig. 3.8). For a given value of energy storage, the rectangular model shows the lowest output power as its sharp MPP point makes it sensitive to even small values of current ripple. The four-diode and the non-linear model give similar results apart from at very low values of energy storage. The three curves show a similar trend : a relatively constant output power at high values of energy storage, with the output power dropping sharply for energy storage values below about 5 mJ/W.

Fig. 4.6(b) shows the variation of the grid current THD with the energy storage for the rectangular and 4-diode PV array models. The THD is roughly proportional to the input current ripple and hence inversely proportional to the energy storage. The rectangular model shows a slightly higher value of THD than the four-diode model for a given value

TABLE 4.3: Normalised ideal grid-connected CSI waveforms for each different stage as a function of energy storage. The nominal modulation index is 0.85 and the 4-diode model is used as the PV model under nominal conditions.



of energy storage. Based on this result, an energy storage value of 12 mJ/W was found to give a value of THD which was below the 5% limit. This value is also shown on Fig. 4.6(a) as vertical line where it is found that the corresponding power reduction is around 1%.

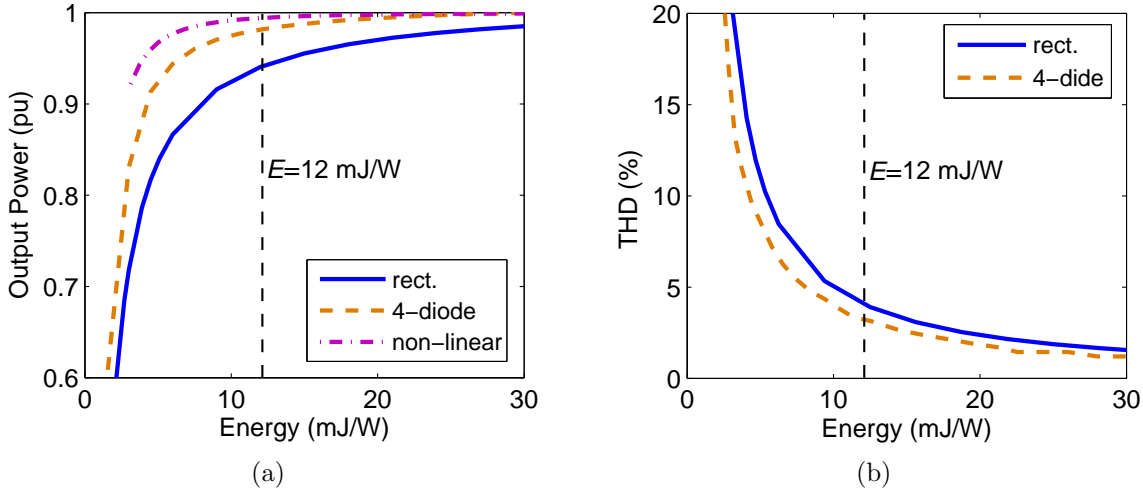


FIGURE 4.6: (a) Normalised output power versus energy storage using rectangular, 4-diode and non-linear models and (b) THD vs. energy storage using rectangular and 4-diode models under nominal conditions.

4.3.4 Effect of Modulation Index

In this section the behaviour of the simplified GC CSI were examined where the output power is varied using the modulation index to be at a nominal m_A of 0.85, an energy storage value of 12 mJ/W and a constant irradiance. The effect of varying the irradiance is shown in the next section.

Fig. 4.7(a) shows some of the operating points including MPP on the I-V curve obtained by changing the modulation index. The corresponding output power versus modulation index curve without any irradiance variation is given in Fig. 4.7(c).

Point B in the figures corresponds to the MPP where the m_A is 0.85. As the modulation index is reduced, the operating points in Fig. 4.7(a) move into the constant-current portion of the PV characteristic and the output power falls linearly with the m_A .

Point A in the figures corresponds to about 20% output power. If the modulation index is increased beyond the MPP value of 0.85, the operating point moves into the

constant-voltage portion of the PV characteristic and the output power falls (see Point C corresponding to a m_A value of unity).

Fig. 4.7(c) also compares the effect of using a rectangular versus 4-diode model for the PV panel. The rectangular model shows a sharp, triangular MPP peak, while the 4-diode model shows a much more rounded peak which is less sensitive to MPP tracking errors.

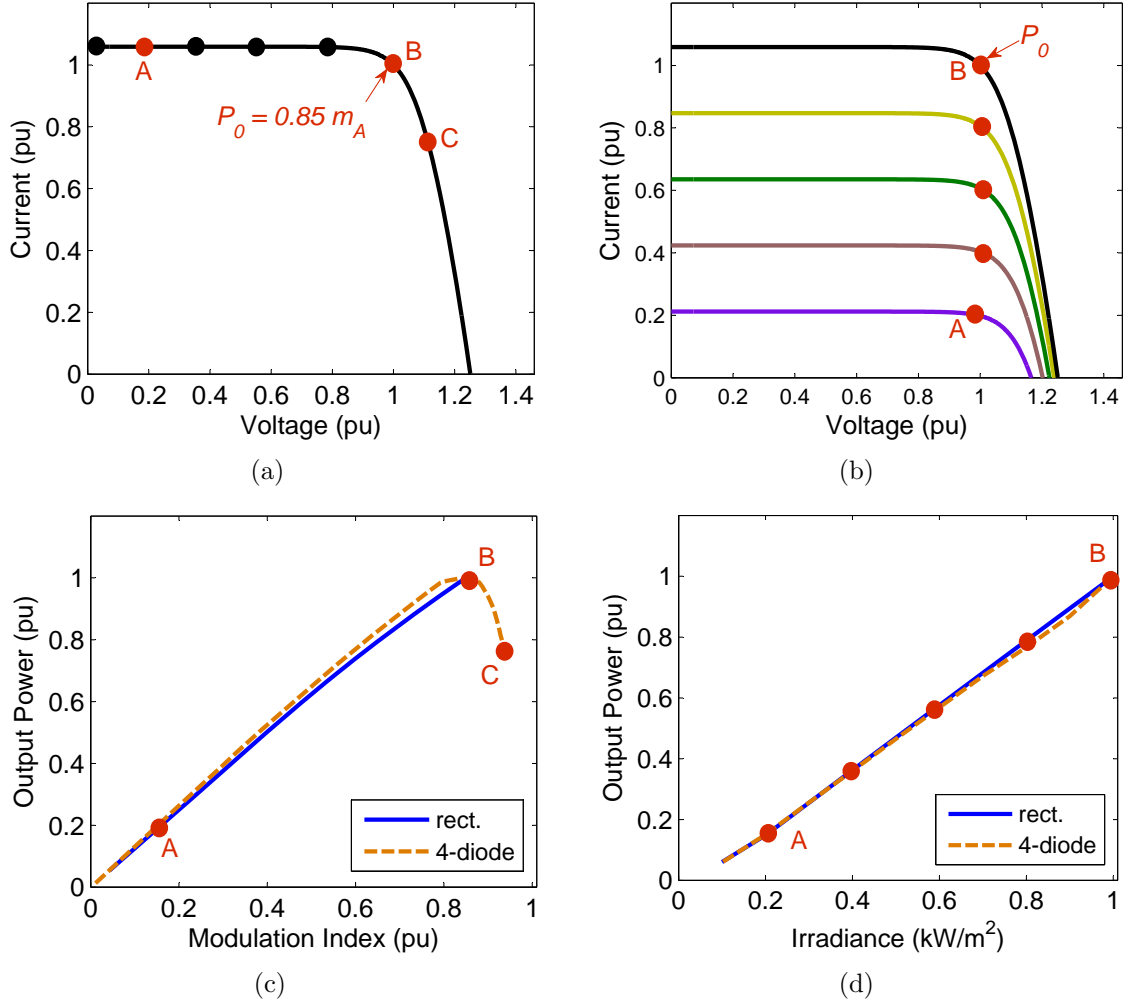
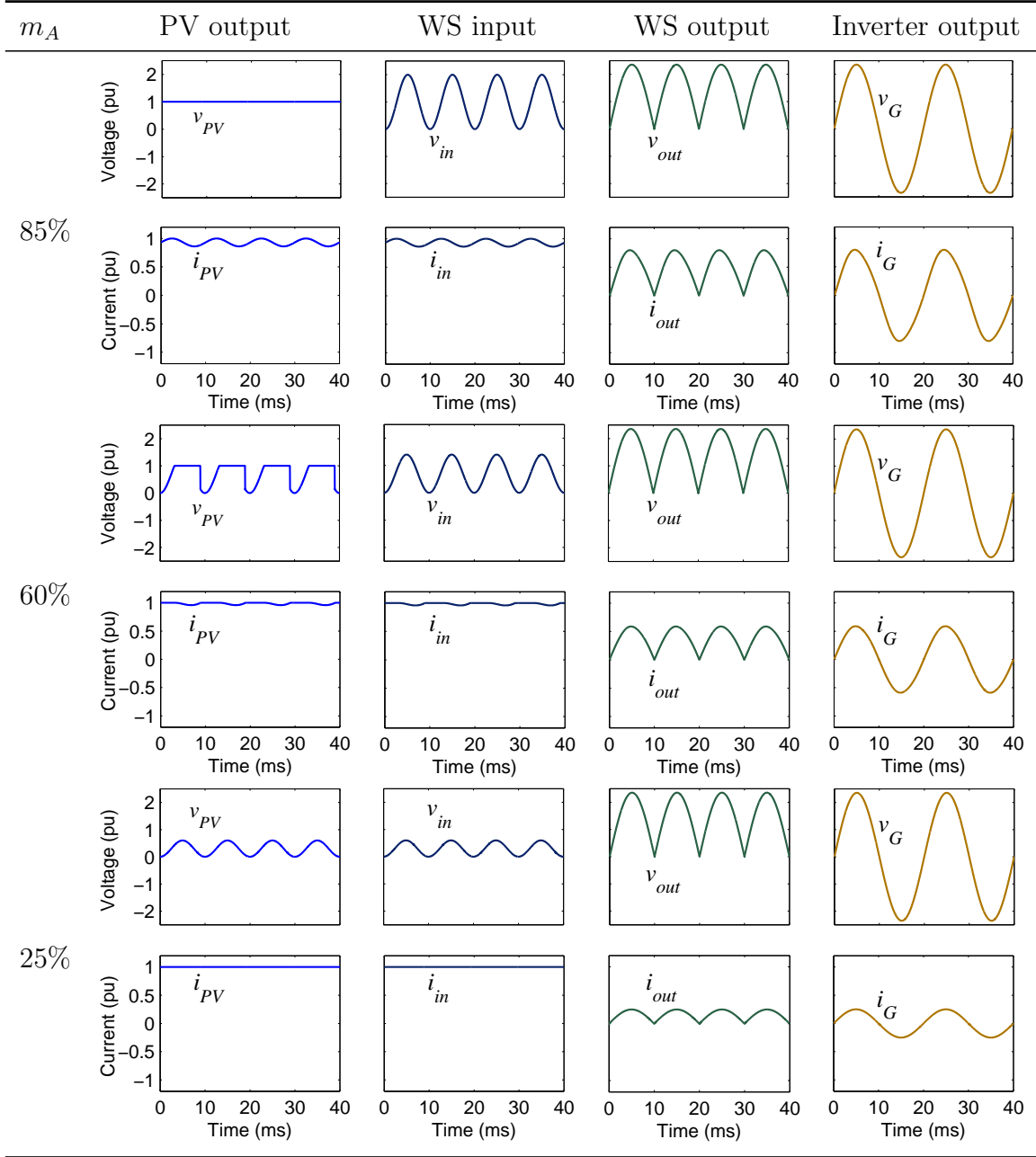


FIGURE 4.7: PV array voltage vs. current curves showing operating points for varying (a) m_A and (b) G values. Output power vs. (c) m_A and (d) G values for both rectangular and 4-diode models.

Tables 4.4 and 4.5 are given to show the inverter voltage and current and voltage waveforms for different values of m_A for the rectangular model and the 4-diode model respectively. The second case in Table 4.3 and the first case in Table 4.5 correspond to 4-diode model (12 mJ/W with nominal m_A of 0.85).

TABLE 4.4: Rectangular PV array model as a function of modulation index. Normalised ideal grid-connected CSI waveforms for each stage where the DC link inductor has 12 mJ/W energy storage capacity, the nominal m_A of 0.85 and irradiance is at its nominal value.



As the modulation index is reduced, (4.7) indicates that the average output voltage of the PV array must decrease proportionally. This causes the PV array to operate more in the current-source region of its I-V curve and causes the PV array output current ripple to decrease but its output voltage ripple to increase.

As the modulation index is reduced, the PV array operates increasingly in the constant-current region and the current ripple decreases. As the DC link inductor voltage drop is proportional to the rate of change of the current, this causes the PV array output voltage and the wavershaper input voltage to become more similar. At low values of modulation index (e.g. 25%), the current ripple becomes zero causing the DC link voltage drop to become zero and the PV array output voltage and wavershaper input voltage to become equal. In this case the DC link inductor has no effect on the circuit.

The effect of the modulation index reduction on the PV array waveforms is illustrated in Fig. 4.8 for the rectangular model. Starting from the top right curve, this shows the wavershaper input voltage waveforms for the nominal m_A (85%) and for a lower value (60%).

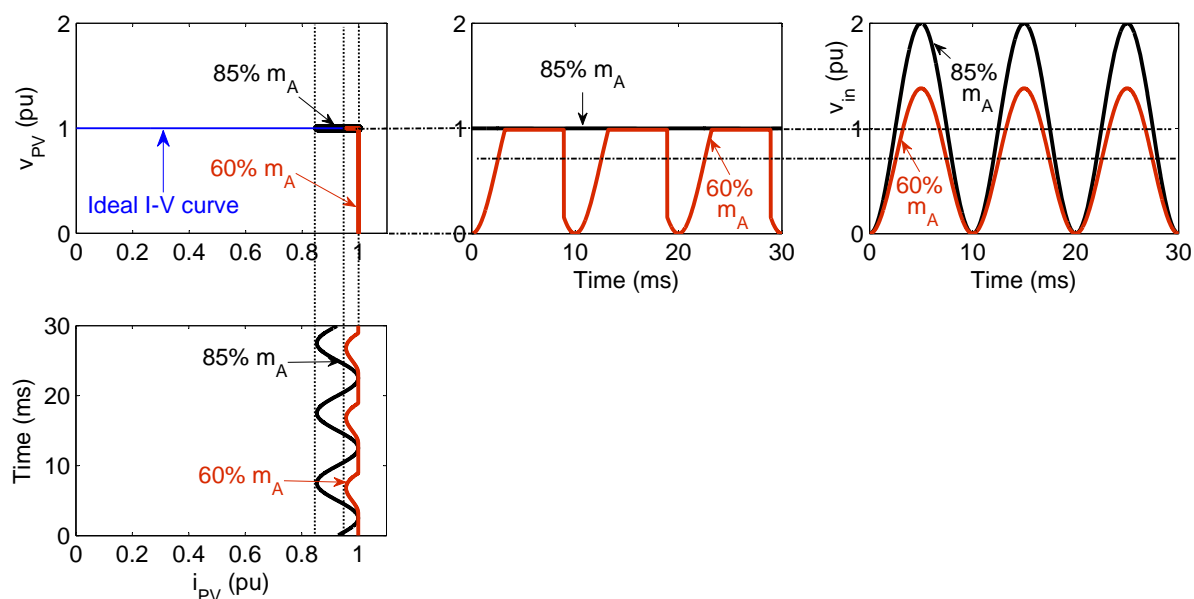


FIGURE 4.8: *Effect of modulation index changes on PV array operating point. Starting from the top right curve and moving left and then downwards : wavershaper input voltage versus time, PV array output voltage versus time, PV array voltage versus current characteristic and PV array output current versus time. Two cases are shown for 85% m_A and 60% m_A .*

As expected from (4.7) the reduction in the modulation index scales the input voltage proportionally. With nominal m_A , the average input voltage of the wavershaper is unity and so the average PV output voltage must also be unity (due to the DC link inductor). Thus PV array operates entirely in the constant voltage region of the I-V curve (shown in the top left curve) with a constant output voltage (top middle curve) and an output current which shows a large amount of ripple (bottom left curve).

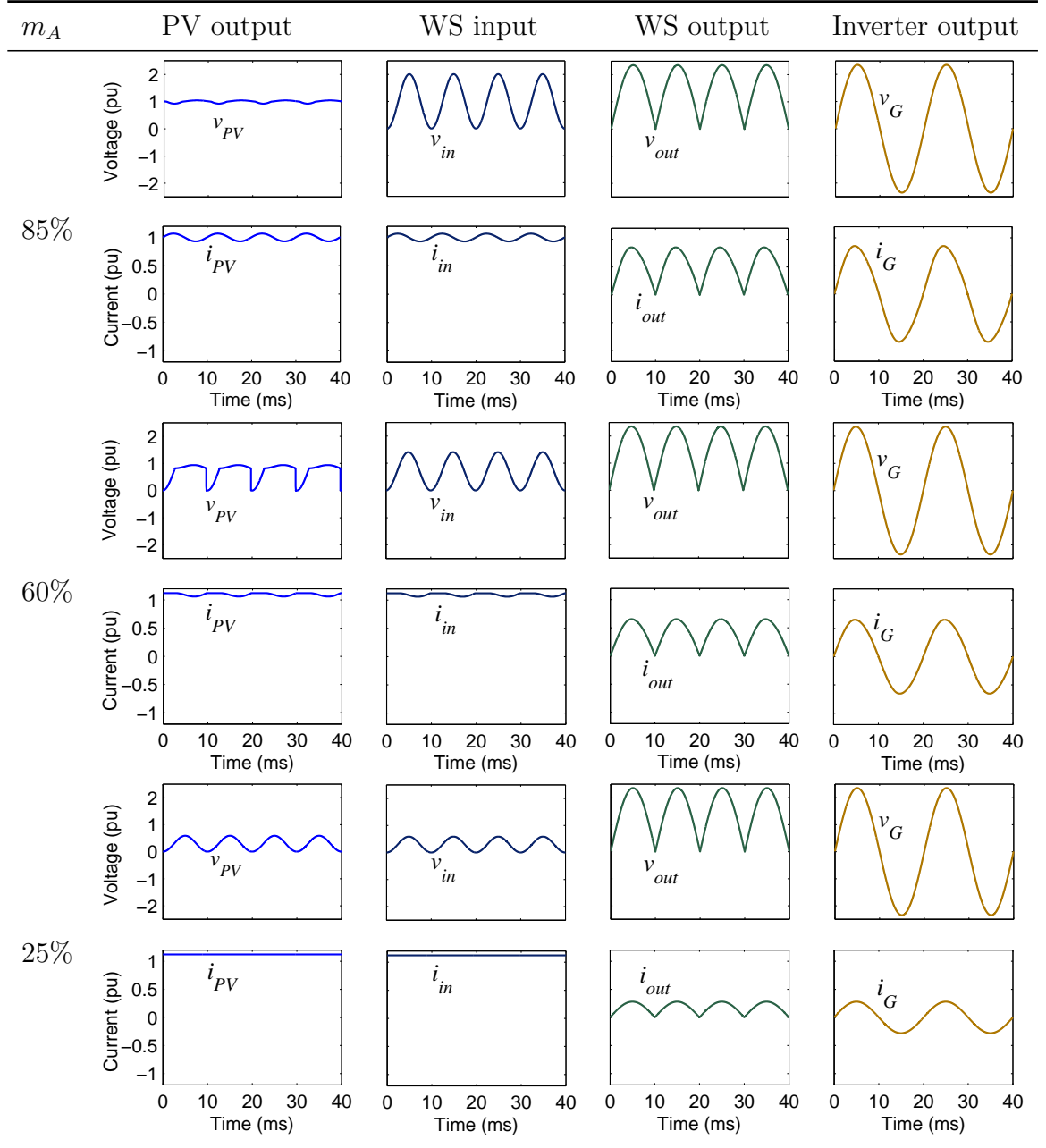
For the lower value of modulation index, the average waveshaper input voltage is less than unity. This causes the PV array to operate partly in the constant voltage and partly in the constant current regions which is evident from the corresponding voltage and current waveforms. It should be noted that with the lower modulation index the current ripple decreases significantly though the voltage waveform has much larger ripple.

The waveforms using the 4-diode model in Table 4.5 are similar to the rectangular model results shown in Table 4.4 with small differences in the PV array output current and voltage waveforms. The rounded knee of the 4-diode model produces smoother PV output voltage waveforms with slightly more current ripple. It also means that the peak voltage and current can slightly exceed unity.

The output current and hence output power is proportional to the modulation index. The output current THD is proportional to the PV array current ripple and thus would be expected to be zero at low values of modulation index but to increase rapidly as the PV array operating point moves into the constant voltage region.

Fig. 4.9 shows the simulated output current THD and PF of the CSI versus normalised output power (obtained by varying the modulation index) for the rectangular and 4-diode PV array models. As the modulation index is increased from zero, the output power increases linearly and the THD follows the expected curve. The output power peaks with the nominal modulation index of 0.85. Increasing the modulation index beyond this results in lower output power (as the PV array output voltage is increased beyond the MPP value) and higher THD (as the current ripple increases). The power-factor graph shows near unity power-factor operation over the entire operating region as expected.

TABLE 4.5: 4-diode PV array model results as a function of modulation index. Normalised ideal grid-connected CSI waveforms for each different stage where the DC link inductor has 12 mJ/W energy storage capacity and the nominal m_A is 0.85 and irradiance is at its nominal value.



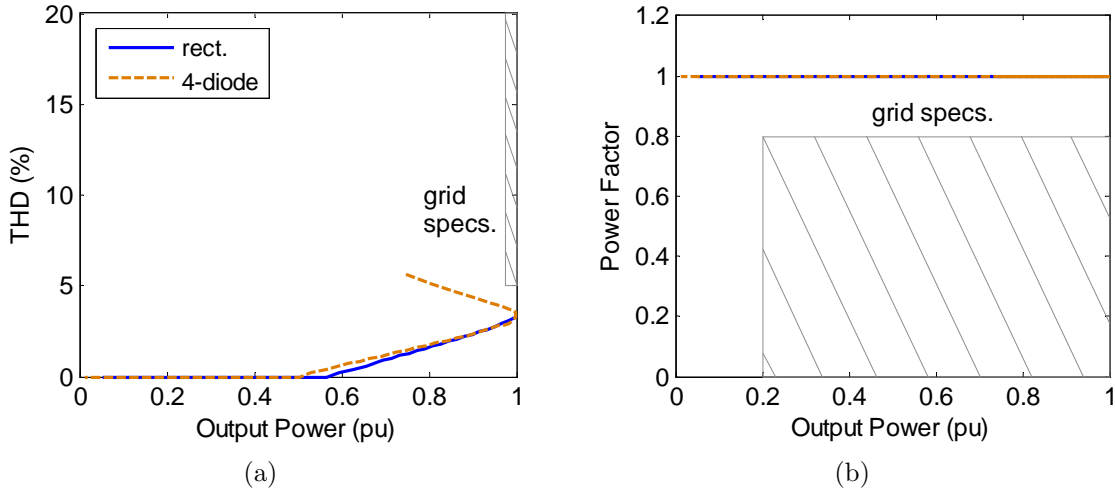


FIGURE 4.9: (a) *THD* and (b) *power factor* as a function of normalised inverter output power using rectangular and 4-diode models where the DC link inductor has 12 mJ/W energy storage capacity, the nominal m_A is 0.85 and irradiance is at its nominal value.

4.3.5 Effect of Irradiance

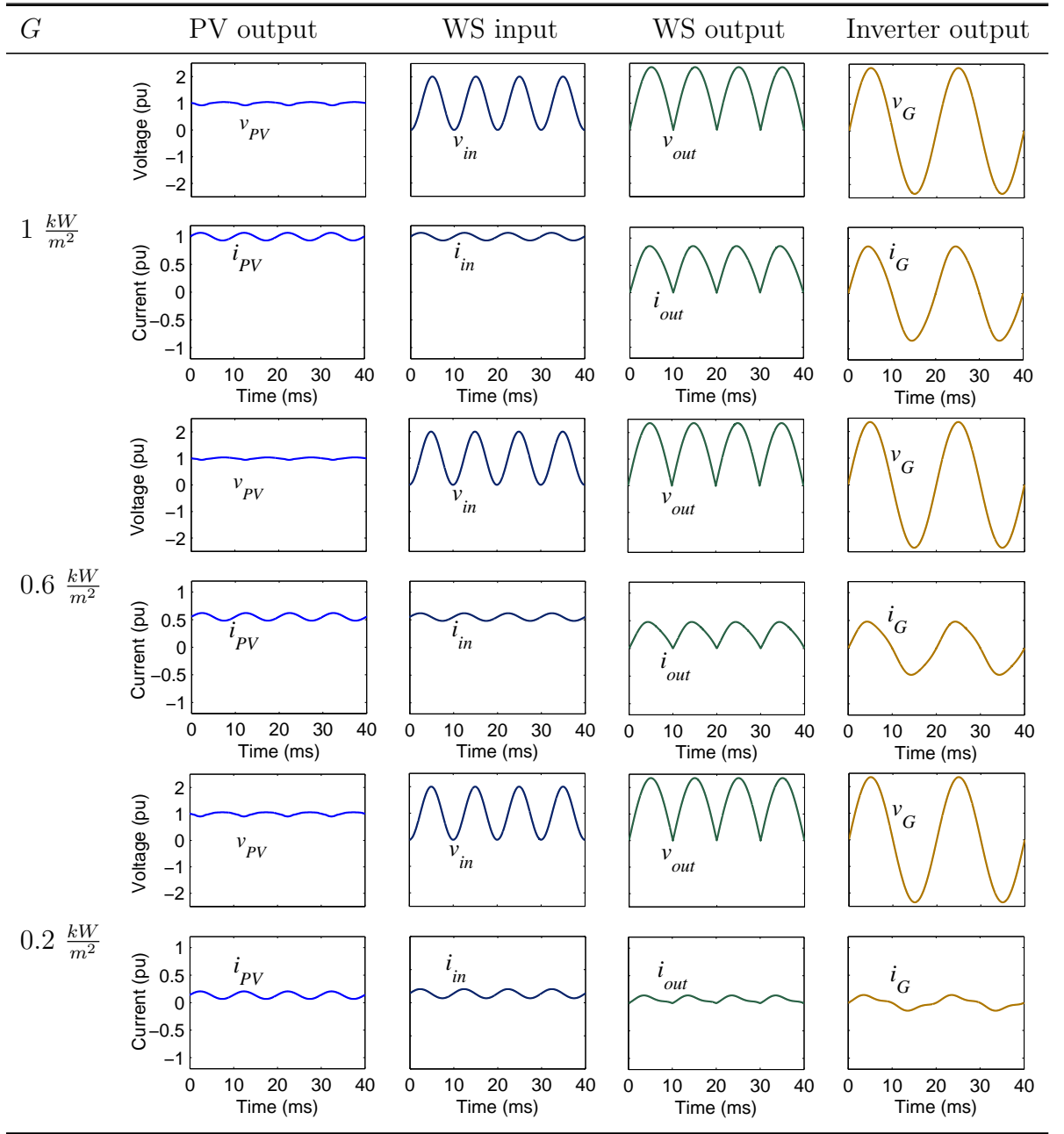
The previous section examined the variation of the output power of the inverter by changing the modulation index under constant irradiance conditions. However a more realistic case for a PV system is to consider the variation of the output power due to irradiance variations where the modulation index is controlled to maximise the output power at each value of irradiance. This section assumes the nominal m_A of 0.85 under nominal irradiance conditions and an energy storage value of 12 mJ/W. The effects of irradiance variations on the PV array I-V curve (see Fig. 4.7(b)) and the corresponding output power versus irradiance curve (see Fig. 4.7(d)) are illustrated. The PV array current is directly proportional to irradiance while the MPP output voltage shows only small changes with irradiance. This means that the output power is nearly proportional to irradiance (Fig. 4.7(d)), and also that the MPP tracking algorithm does not need to vary the modulation index significantly except at low irradiance values.

The normalised waveforms of the GC CSI are provided in Table 4.6 using the 4-diode model for the PV array. Compared to the varying modulation index case shown in Table 4.5, the first case in each table (maximum output power) are identical as they correspond to nominal conditions ($G = 1 \text{ kW/m}^2$ and $m_A = 0.85$). In Table 4.6, as the irradiance is reduced, the average PV output current reduces proportionally while the average PV output voltage remains relatively constant. This is in contrast with the

varying modulation index case (Table 4.5) where as the output power is reduced the average PV output current stays relatively constant and the average PV output voltage reduces proportionally to the output power.

An important observation from the varying irradiance case shown in Table 4.6 is that the output current THD increases substantially at low output powers. This is visible in the 0.6 kW/m² case but even more obvious in the 0.2 kW/m² case. This effect is opposite

TABLE 4.6: Normalised ideal grid-connected CSI waveforms for each different stage as a function of irradiance with the 4-diode model. The DC link inductor has 12 mJ/W energy storage capacity and the nominal m_A is 0.85 under nominal conditions.



to what was observed with varying modulation index case in Table 4.5 where the THD is reduced at low output powers. This difference is due to the PV array output current waveform. As the output power is reduced, in the varying modulation index case the PV array output current stays close to the rated short-circuit current and has a ripple component which reduces with output power. In contrast, in the varying irradiance case, the average PV current reduces as the irradiance is reduced however the ripple component has a relatively constant ripple amplitude. Thus at low values of irradiance, the ripple amplitude becomes large with respect to the average current and this results in high output current distortion.

The increased THD at low values of irradiance is likely caused by the reduction in the ratio of energy storage to output power. This effect was studied earlier in Table 4.3 and Fig. 4.6 under the maximum power conditions which showed that the THD was roughly inversely proportional to the ratio of energy storage to output power. Note under varying irradiance conditions the output power is directly proportional to the average PV array output current while the amount of stored energy is proportional to the square of the average PV array output current. As a result the ratio of energy storage to the output power falls inversely with output power and hence the THD should be roughly inversely proportional to output power.

Fig. 4.10 shows the THD and PF curves of the GC CSI as a function of output power obtained by varying the irradiance, for different E values ranging from 3 mJ/W to 24 mJ/W (at rated output power). The curves are shown for the 4-diode PV model with the curves for the rectangular model for the 12 mJ/W case shown for reference. The results for the two PV models show similar results except at low values of output power. As expected the THD values are inversely proportional to both output power and the value of E at rated output power. The exceptions to this are at low values of output power (below about 20%) and for low values of rated energy storage (e.g. 3 mJ/W). A value of 12 mJ/W or above is required to meet the 5% grid THD requirement.

The power factor curves in Fig. 4.10(b) meet the grid requirements for all energy storage values. The PF shown is affected by both the phase-shift of the fundamental current component and the total harmonic distortion of the current waveform. The fundamental PF remains near unity in these cases and so the small reduction in PF is largely caused by the effect of THD. Note when the effect of the grid output filter is considered in

the next chapter, this will result in substantial reduction in the fundamental PF at low output powers.

Fig. 4.10(c) shows THD for different irradiances using several E values as in Fig. 4.10(a) employing FFD control approach. The harmonic content in Fig. 4.10(a) is predominately caused by 100 Hz ripples. The FFD control removes the fluctuations as if the WS input current purely constant. Hence there is no THD presence in Fig. 4.10(d). For only 3 mJ/W case below about 20% output power, inconsiderable amount of THD (0.2%) is seen due to large ripple in the PV array output current as seen in Table 4.3. As the effect of the THD is significantly reduced using FFD control, the PF is unity for all irradiance and different energy storage capacity cases as seen in Fig. 4.10(d).

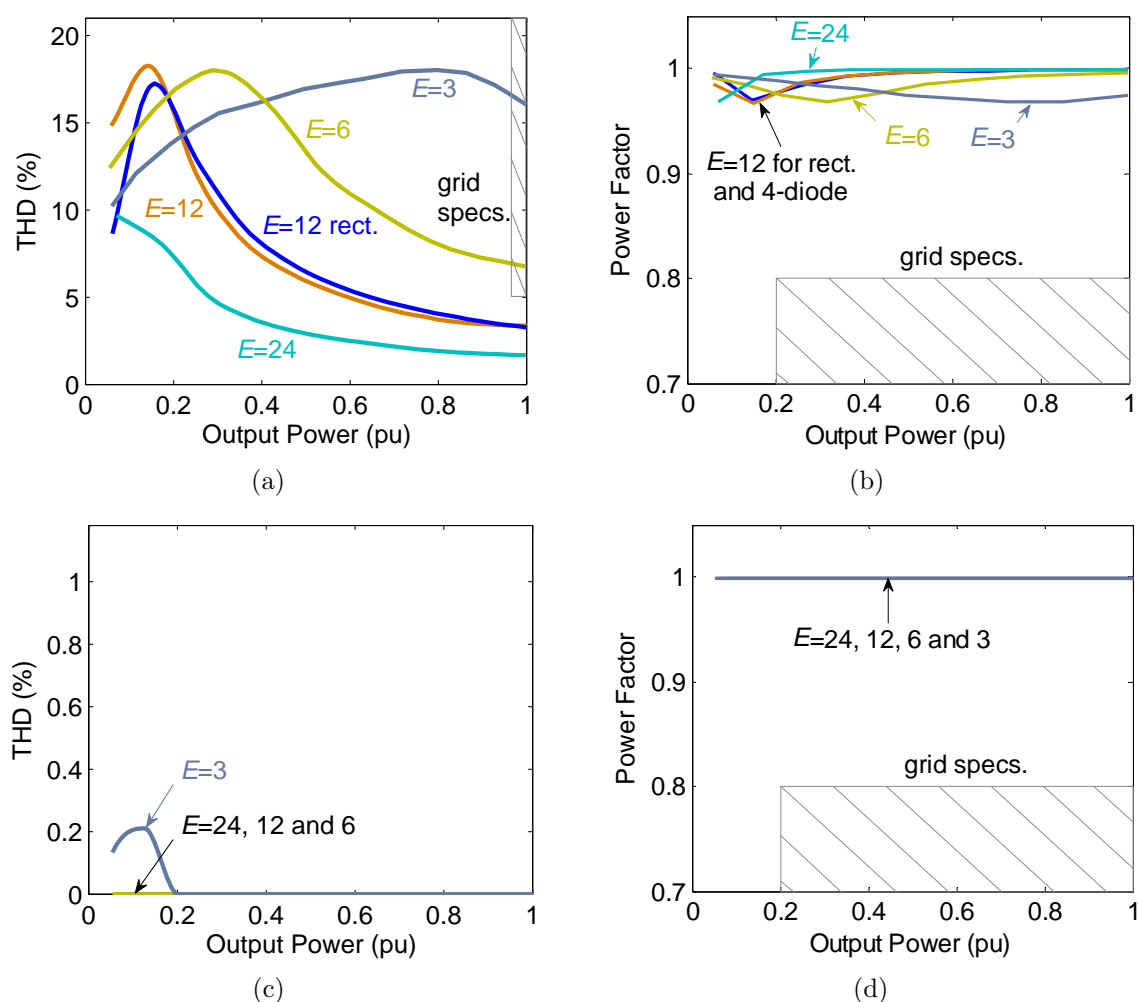


FIGURE 4.10: (a) THD and (b) PF vs. normalised inverter output power for the varying irradiance case for rated energy storage values of 3, 6, 12 and 24 mJ/W. The 4-diode PV model case is used. For comparison the THD with the rectangular PV model is also shown for the energy storage value of 12 mJ/W case. FFD control implementation of the same graphs (c) THD and (d) PF .

4.4 Summary

A simplified model of the proposed grid-connected current-source inverter neglecting PWM switching and assuming ideal components was simulated to gain a better understanding of its operation and performance. The voltage and current waveforms were examined in each stage of the circuit. The selection of the ratio of the peak grid voltage to the PV panel rated output voltage (that is, the nominal m_A) was discussed taking into account the effect of temperature variations. A value of 0.85 was recommended.

The design of the inverter to meet the PF and THD requirements of the Australian Standards was also covered using simulations. As part of this the following were examined : selection of the amount of DC link energy storage, the use of rectangular versus 4-diode PV array models, and the effect of output power variation by changing both modulation index and the irradiance. It was found that at least 12 mJ/W of energy storage under rated conditions is recommended and that varying irradiance case produced significantly larger values of THD at low values of output power but still could meet the Australian Standards.